Received: 6 May 2020 | Accepted: 13 December 2020

DOI: 10.1002/vzj2.20104

Vadose Zone Journal

ORIGINAL RESEARCH ARTICLE

Soil hydraulic interpretation of nuclear magnetic resonance measurements based on circular and triangular capillary models

Stephan Costabel[1] | **Thomas Hiller**[2]

[1] Department of Groundwater and Soil Science, Federal Institute for Geosciences and Natural Resources, Wilhelmstrasse 25-30, Berlin 13593, Germany

[2] Department of Geoelectrics & Electromagnetics, Leibniz Institute for Applied Geophysics, Stilleweg 2, Hanover 30655, Germany

Correspondence
Stephan Costabel, Department of Groundwater and Soil Science, Federal Institute for Geosciences and Natural Resources, Wilhelmstrasse 25-30, 13593 Berlin, Germany.
Email: Stephan.Costabel@bgr.de

Assigned to Associate Editor Ute Wollschläger.

Abstract

Geophysical nuclear magnetic resonance (NMR) applications are used to estimate pore size distributions (PSDs) of rocks and sediments. This is commonly realized by empirical calibration using information about the surface-to-volume ratio of the material. Recent research has developed joint inversion concepts for NMR relaxation data that provides the PSD with a minimum of information. The application requires the NMR signal of a sample at saturation and at least one at partial saturation and at known suction. The new inversion concept physically simulates the desaturation process as part of the forward operator. The cross-section of the model capillaries in the underlying bundle can be either circular or triangular. Our study investigates the performance of the NMR joint inversion to predict water retention function (WRF) and capillary-based hydraulic conductivity (K_{cap}) as functions of saturation for different sands. The angularity of the pores has no significant impact on the estimated WRF but affects the K_{cap} estimation significantly. Our study shows that the WRF is predicted reliably for sand samples under fast diffusion conditions. The K_{cap} estimations are also plausible but tend to systematic overestimation, for which we identified the tortuosity being the main reason. Because NMR relaxation data generally do not provide tortuosity information, a plausible tortuosity model remains an issue of classical calibration. Further development of the approach will thus consider tortuosity measurements (e.g., by electrical resistivity measurements and/or gradient NMR) and will consider the relaxation mechanisms outside fast diffusion conditions to enhance its applicability for coarse soils.

1 | INTRODUCTION

Quantifying the soil hydraulic functions is challenging. The water retention function (WRF) of soil samples can be measured exactly by controlled drainage and/or imbibition experiments, which is a time-consuming and effortful procedure (Bittelli & Flury, 2009; Warrick, 2003), whereas the unsaturated hydraulic conductivity (K_U) as a function of water content or pore pressure has to be estimated empirically from the data of such experiments. Using the evaporation method, water retention (WR) measurements are performed with much faster progress, and K_U can be estimated from the vertical pressure gradient and moisture flux inside the

Abbreviations: CS, coarse sand; FJI, fixed joint inversion; FS, fine sand; LLS, linear least square; MS, medium sand; MSFS, medium and fine sand; NMR, nuclear magnetic resonance; PSD, pore size distribution; RTD, relaxation time distribution; VG, van Genuchten; VGM, van Genuchten–Mualem; WR, water retention; WRF, water retention function.

sample (Peters & Durner, 2008; Peters, Iden, & Durner, 2015). However, the corresponding K_U values for a certain soil sample are only available for a limited range of pore pressures (above −2,000 hPa), and information on a possible hysteresis of the WRF is in general not available. From sample to technicum scale (e.g., column experiments), multistep-outflow and/or inflow experiments in combination with numerical hydraulic simulations allow the quantification of WRF and K_U by inverse modeling (Nasta, Huynh, & Hopmans, 2011; Schaap, Shouse, & Meyer, 2003; Šimůnek & van Genuchten, 1999), where unsuitable WRF and K_U models can cause systematic errors that cannot be identified easily. Rapid measurement systems providing WR information such as the dew point method (Campbell, Smith, & Teare, 2007) or psychrometers (Skierucha, 2005) are only available in the dry range at capillary pressures below −10,000 and −1,000 hPa, respectively. Regarding the general necessity in soil physics to acquire and investigate huge sets of samples to hydraulically characterize an area of interest, fast and convenient methods for measuring or estimating WRF and K_U are desired.

Methods of nuclear magnetic resonance (NMR) are seldom applied in soil sciences, although they have great potential for soil hydraulic analyses regarding the challenges described above. Nuclear magnetic resonance applications exhibit a fast measurement progress and are available from sample to field scale. Very well established for hydrocarbon and groundwater exploration, they are used for measuring the volumetric water content, as well as for estimating pore size distribution (PSD) and hydraulic conductivity (Arns, 2004; Kenyon, 1997; Knight et al., 2015; Mohnke & Yaramanci, 2008; Vouillamoz et al., 2008). For the latter two, empirical approaches or semiempirical models based on simple pore geometries are used that have to be calibrated for a specific kind of rock material or sediment. The feasibility of NMR relaxometry for estimating soil hydraulic parameters was investigated, for example, by Ioannidis, Chatzis, Lemaire, and Perunarkilli (2006), Jaeger, Bowe, van As, and Schaumann (2009), Stingaciu et al. (2010), and Costabel and Yaramanci (2011, 2013).

In rock and soil physics, pore model descriptions with robust physical bases have been developed. In contrast with pure empirical models, they have a more general applicability and allow the prediction of the hydraulic properties inside single pores, as well as whole pore systems over several magnitudes of pore sizes (Hammecker, Barbiero, Boivin, Maeght, & Diae, 2004; Or & Tuller, 2000; Øren, Bakke, & Arntzen, 1998; Tuller, Or, & Dudley, 1999). For instance, pore models based on capillaries with angular cross sections allow a physical description of the WRF hysteresis and can provide K_U estimates for a large variety of soils with different texture and structure (Mason & Morrow, 1991; Ransohoff & Radke, 1988; Tuller & Or, 2001). Nuclear magnetic resonance-related research has shown that these kinds of pore models are also capable to describe unsaturated NMR data (Costabel, 2011; Mohnke, Jorand, Nordlund, & Klitzsch, 2015). They allow the coupling of NMR and pore pressure measurements during data inversion and interpretation (Hiller, 2020; Hiller & Klitzsch, 2018) to estimate the PSD and correspondingly the pore pressure curves of porous material. So far, the performance of this kind of NMR data interpretation has not been investigated and assessed for natural sediments and soils. As a first step, we study in this work the impact of the consistent implementation of circular and triangular capillaries on the NMR-based estimation of WRF and K_U. We use the joint inversion approach suggested by Hiller and Klitzsch (2018) to provide the PSD and the surface relaxivity of sand samples. Based on the estimated PSD, we compute the WRF according to the formalism suggested by Peters (2013) and the capillary-based K_U (K_{cap}) according to the desaturation model of Tuller and Or (2001) for circular and triangular capillary pore bundles. To consider the entire distribution of measured pore sizes, we suggest and investigate two different upscaling approaches: the hydraulic parallel connection of all capillaries in the bundle and the use of an effective apparent capillary. Our analysis comprises numerical and real NMR data. For the latter, we use sand samples of different grain sizes. The sample material has been used already by Costabel and Yaramanci (2011), who combine NMR and drainage measurements in column experiments. They show that the relative T_2 time of unsaturated sand is correlated with its relative hydraulic conductivity K_{rel}. The power–law relationship between these two quantities can be used to provide K_{cap} estimates from NMR relaxation measurement for partially saturated sand samples if adequate calibration data are at hand: the T_2 time of the sample at saturation and the saturated hydraulic conductivity. In this study, we want to investigate the idea of predicting WRF and K_{cap} from the relaxation time distribution (RTD) of the saturated sample. In particular, we want to study the effect of the angularity of the assumed capillary cross-section on the estimation of WRF and K_{cap}.

Core Ideas

- Triangular capillaries can explain NMR data of sand better than circular ones.
- NMR joint inversion combines data inversion and hydraulic desaturation of the pore space.
- NMR joint inversion yields the pore size distribution without empirical calibration.
- The suggested approach can provide estimations of WRF and K_{cap} for sandy soils in the fast diffusion range.

2 | THEORETICAL BACKGROUND

2.1 | NMR in porous media

The principle of the NMR method for water-saturated porous material is based on the spin-related magnetic moment of the ^{1}H nuclei in the pore water molecules. An ensemble of ^{1}H spins forms a macroscopic magnetization that is aligned with the predominant external magnetic field. During the NMR experiment, the spin magnetization is manipulated by a series of electromagnetic pulses, and an exponential response signal is measured that represents the relaxation of the spin system back to the equilibrium state. In this study, we focus solely on the so-called transverse (or T_2) relaxation (Behroozmand, Keating, & Auken, 2014; Dunn, Bergman, & Latorraca, 2002). When observed in porous media, the relaxation process of the pore water is accelerated compared with free water due to the fast energy exchange of the ^{1}H spins with the pore walls: the smaller the dimension of a single pore, the smaller the individual relaxation time of this pore. When observing materials with a significant distribution of different characteristic pore sizes, the NMR signal E (in V) as function of the measurement time t (in s) consequently exhibits a multiexponential relaxation behavior:

$$E\ (t) = \sum_i I_i \exp\left(-\frac{t}{T_{2i}}\right) \tag{1}$$

where I_i (same unit as E) and T_{2i} (in s) are the individual intensity and relaxation time of the ith pore regime, usually associated with a certain pore size. The multiexponential character described with Equation 1 is the key of NMR applications in geo- and petrophysics: the reconstruction (i.e., inversion) of the complete RTD from the measured signal of a rock or soil sample (i.e., I_i as a function of T_{2i}) leads to an estimation of its PSD. Details can be found for instance in Dunn et al. (2002) and Behroozmand et al. (2014). The sum over I_i is proportional to the water content in the sample, and thus, the saturation state of a sample can easily be determined from NMR by

$$S = \frac{E^{ps}(t=0)}{E^{s}(t=0)} = \frac{\sum_i I_i^{ps}}{\sum_i I_i^{s}} \tag{2}$$

with "s" and "ps" being the indices for the NMR measurements for the saturated and the partially saturated sample, respectively.

In general, the T_2 relaxation rate inside porous media is given by

$$\frac{1}{T_2} = \rho_2 \frac{S_w}{V_w} + \frac{1}{T_{Bulk}} + \frac{1}{T_{Diff}} \tag{3}$$

where S_w and V_w are the water-wetted pore surface (m^2) and the water-filled pore volume (m^3), respectively, and ρ_2 is the surface relaxivity (m s^{-1}), a material-specific parameter that describes how fast the energy between proton spins and pore surface is exchanged on average throughout the pore space. The rates $1/T_{Bulk}$ (bulk relaxation) and $1/T_{Diff}$ (diffusion relaxation) describe the relaxation inside the pore water (i.e., without the influence of the pore surface) and the relaxation component due to the self-diffusion of the water molecules through a gradient magnetic field, given that the predominant magnetic field is not homogeneous (Dunn et al., 2002; Keating & Knight, 2008). Although these two relaxation components are independent of the pore geometry and size relations and thus not relevant for estimating the hydraulic properties of the pore space, they have to be considered for a correct reconstruction of the PSD.

It is worth noting that Equation 3 is only valid if the investigated pore space is in the so-called fast diffusion regime. This means that the diffusional exchange of proton spins during the relaxation process is fast enough, so that the energy exchange between all excited proton spins and the pore walls can be considered to be the same on average. This is not the case for material with large pores and/or high ρ_2, where additional relaxation modes appear at short times and the relationship between NMR relaxation time and S_w/V_w is becoming nonunique (Brownstein & Tarr, 1979; Costabel, Weidner, Müller-Petke, & Houben, 2018; Müller-Petke, Dlugosch, Lehmann-Horn, & Ronczka, 2015).

2.2 | NMR responses of saturated and nonsaturated circular and triangular capillaries

In this study, we consider capillary pores with circular and triangular cross sections (see Figure 1). Consequently, the surface-to-volume ratio S_w/V_w (Equation 3) for a single saturated capillary is determined to be the ratio of its perimeter P_0 and its cross-sectional area A_0. It can be described as function of the pore dimension with $P_0/A_0 = a/L$, where a is the geometry factor and the quantity L is a measure of the pore size. In the simplest case of a circular capillary with L being the pore radius r_{circ}, $a = 2$. For capillaries with noncircular cross-sections, a suitable L has to be defined first (e.g., side length of the equilateral triangle or length of hypotenuse for the right-angled triangle), which determines the corresponding a. Table 1 lists the resulting equations for S_w/V_w for all pore geometries considered in this study.

The geometry factor of angular capillaries generally increases with increasing angularity. To compare the NMR responses of capillaries of different shape, Hiller and Klitzsch (2018) reasonably suggested considering the equivalent pore radius r_{eq}: a pore with arbitrary shape is characterized by the radius of a circle (r_{eq}) with identical cross-sectional area (A_{eq}). As an example, we consider three pores with

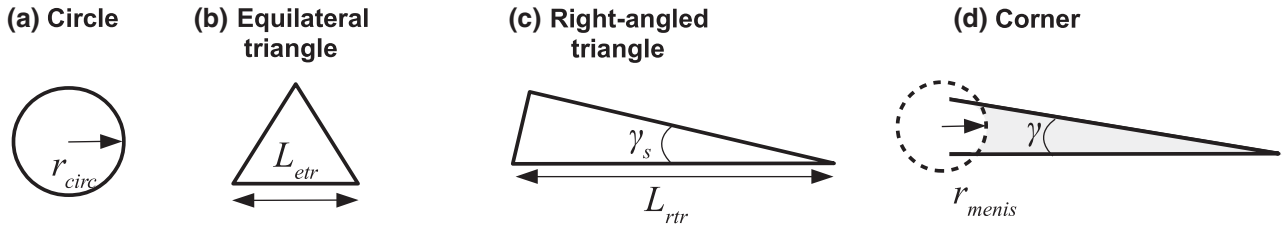

FIGURE 1 Pore geometries (i.e., capillary cross-sections) considered in this study

TABLE 1 Pore geometries considered in this study (see also Figure 1) and their corresponding equations regarding the nuclear magnetic resonance (NMR)-relevant pore surface-to-volume-ratio S_w/V_w and permeability $k = (1/\kappa)L^2$, where κ is the nondimensional flow resistance parameter and L is the relevant pore dimension of the different capillary cross sections: radius r_{circ} of the circle, side length L_{etr} of the equilateral triangle, length of the hypotenuse L_{rtr} of the right-angled triangle, and radius r_{menis} of the interface arc meniscus in a corner

Pore structure	Circle	Equilateral triangle	Right-angled triangle	Corner
$L =$	r_{circ}	L_{etr}	L_{rtr}	r_{menis}
$\frac{S_w}{V_w} =$	$\frac{2}{r_{circ}}$	$\frac{12}{\sqrt{3}L_{etr}}$ [a]	$\frac{2+2\sin(\gamma_s)+2\cos(\gamma_s)}{\sin(\gamma_s)\cos(\gamma_s)L_{rtr}}$	$\frac{P_C}{A_C}$ with $P_C = \frac{2r_{menis}}{\tan(\frac{\gamma}{2})}$ and $A_C = r^2_{menis}[\frac{1}{\tan(\gamma/2)} - \frac{\pi(180-\gamma)}{360}]$
$k =$	$\frac{1}{8}r^2_{circ}$	$\frac{1}{80}L^2_{etr}$	$\frac{3G\sin(\gamma_s)\cos(\gamma_s)}{10}L^2_{rtr}$	$\frac{1}{\varepsilon}r^2_{menis}$ with [b] $\varepsilon(\gamma) = \exp(\frac{b+d\gamma}{1+c\gamma})$

Note. γ_s, sharp angle; γ, corner angle; P_C and A_C, perimeter and cross-sectional area of the meniscus water; G, shape factor with $G = A_0/P^{2_0}$ (see, Patzek & Silin, 2001); b, c, and d, empirical parameters.

[a]Mohnke et al. (2015).

[b]Parameterization of $\varepsilon(\gamma)$ according to Tuller and Or (2001); see the text for details.

identical A_{eq} (= 314.2 μm^2) and r_{eq} (= 10 μm) but different cross-sectional geometry (Figure 2, a–c). The sharp angle γ_s of the right-angled triangle (Figure 2c) was set to 10°. The T_2 times in case of full saturation, calculated for ρ_2 = 10 μm s^{-1} and depicted as dark blue spectral lines in Figure 2d–2f, decrease with increasing angularity.

According to the desaturation model of Mason and Morrow (1991), for each capillary with a certain shape and angularity, an individual critical threshold pressure p_{crit} exists, at which the gas phase enters the pore and spontaneously replaces most of its pore water. In the simple circular case, p_{crit} is inversely proportional to r_{circ} according to the Young–Laplace equation (see, e.g., Hiller & Klitzsch, 2018; Tuller et al., 1999), meaning if p_{crit} is reached, the pore water is completely removed by the invading air. Tuller et al. (1999) and Tuller and Or (2001) also consider adsorbed water films in their model that reside on the pore walls after the air invasion. However, we do not consider this kind of WR in our NMR modeling approach, because the corresponding theoretical NMR response signals from adsorbed water films (according to the theory in Equation 3) relax too fast to be captured by common low-field NMR technology.

After air has invaded an angular pore, water is kept in the corners and creates arc menisci due to the interaction of the capillary forces at the pore wall and surface tension of the water (light blue areas in Figures 2b and 2c). The radius r_{menis} of the interface arc meniscus decreases with increasing pore pressure while pore water keeps draining and air continues filling the pore. For an angular pore, p_{crit} depends on its angularity (see Hiller & Klitzsch, 2018; Tuller et al., 1999; Tuller & Or, 2001) and corresponds to a certain critical radius r_{crit}, which equals r_{menis} in the very moment, when the air starts entering the pore. The water remaining in its corners produces NMR signals according to the individual S_w/V_w in each corner—that is, the ratio of its wetted perimeter (P_C) and the residual cross-section filled with water (A_C). The NMR response of a single corner with angle γ can be calculated according to the equations in Table 1. Figures 2d–2f depict and compare (light blue lines) the different NMR responses of each example pore at its individual p_{crit}. In contrast with angular pores, a NMR signal from the completely desaturated circular pore is not captured in this case (Figure 2d),

In case of the equilateral triangle, the signals from each corner superpose in one single spectral line (Figure 2e), whereas in the case of the right-angled triangle, three individual lines appear in the relaxation spectrum (Figure 2f). However, the signal contribution from the two corners with angles >45° is more than tenfold smaller than that of the sharp angle (please note the log scale on the y axes in Figure 2, d–f), and it is expected that this contribution is most likely not measured under realistic conditions.

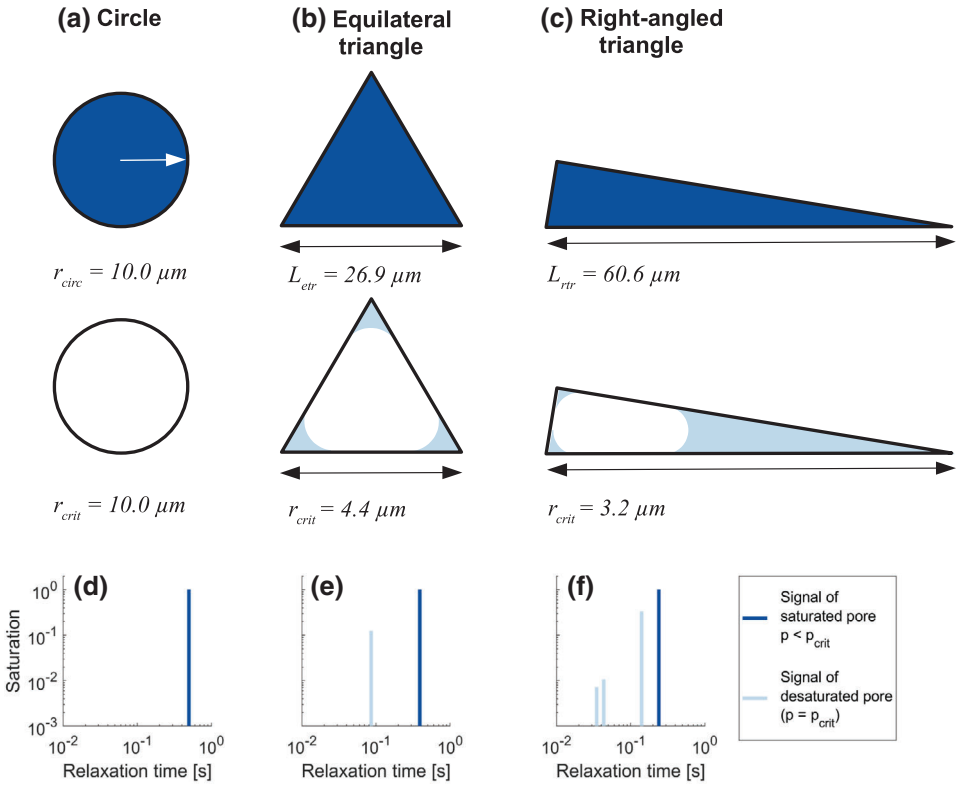

FIGURE 2 Cross-sections of capillaries with identical equivalent radius (r_{eq} = 10.0 µm): (a) circular, (b) equilateral triangle, (c) right-angled triangle with sharp angle $\gamma_s = 10^\circ$. The dark blue color represents the saturated pore, and light blue represents the residual water after reaching the critical pore pressure corresponding to the critical radius r_{crit} of the arc menisci in the corners. Subfigures d–f show the respective nuclear magnetic resonance (NMR) relaxation times as spectral lines for surface relaxivity ρ_2 = 10 µm s^{-1}

2.3 | NMR relaxation time distribution by linear least square inversion

The inversion of multiexponential NMR signals (Equation 1) to reconstruct their RTDs (i.e., the signal intensities of the different pore clusters I as a function of their respective T_2) is usually realized by a linear least square (LLS) minimization algorithm with smoothness constraints to stabilize the numerical calculation (Costabel & Yaramanci, 2013; Dunn et al., 2002). This is reasonable because a more or less continuous PSD is expected for the very most sediments and soils. However, the regularization of these smoothness constraints is somewhat crucial regarding the physical interpretation of the results. Determining the smoothness constraints too tightly, the broadness of the RTD (and consequently that of the corresponding PSD) is overestimated (see Costabel & Yaramanci, 2013). Thus, an adequate criterion for adjusting the smoothness of the RTD is mandatory as discussed in detail below in Section 3.2.

We want to demonstrate how the LLS algorithm works in principle for simulated partially saturated capillary bundles with circular and triangular cross-section and modify our single pore examples from Figure 2 to get a more realistic view on the NMR responses. We consider a lognormal distribution of pores sizes for each observed cross section (circle, equilateral triangle, right-angled triangle) with a mean value of r_{eq} = 10 µm and a standard deviation of σ = 0.2 at the log scale. The area under the distribution equals one. As for the calculations of the single pore responses, the desaturation state is computed for the individual p_{crit} corresponding to r_{eq} = 10 µm (i.e., corresponding to the individual maximum of the distributions). Consequently, all pore sizes smaller than r_{eq} = 10 µm are still completely filled with water, whereas the larger ones are already invaded by air.

Figure 3 shows the resulting RTDs after applying a common smooth LLS inversion to the respective NMR response signals for saturated and desaturated conditions (synthetic noise level: 0.1%). Despite the fact that in each case the residual water saturation is ~0.3, the corresponding spectra exhibit significant differences. In the case of a circular cross-section, the T_2 spectrum of the desaturated pore space lies completely inside the RTD for the full saturation (Figure 3a). In the case of an equilateral triangular cross-section, a bimodal distribution develops with one mode almost completely inside the RTD at saturation and the other one at a T_2 range about a magnitude smaller than the original RTD (Figure 3b). The

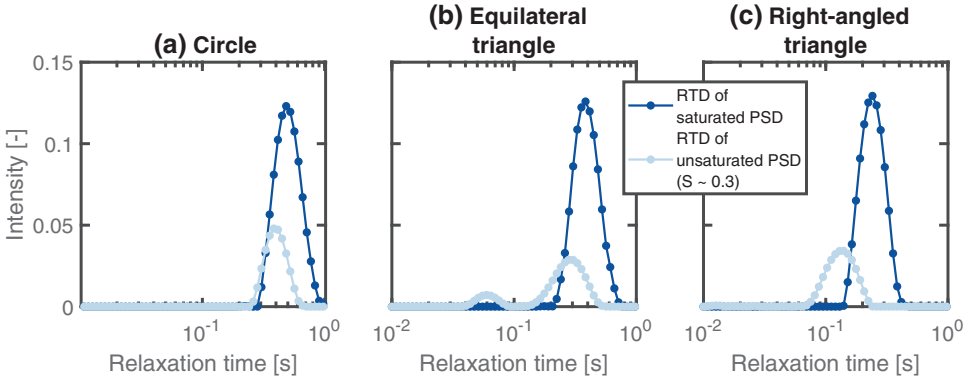

FIGURE 3 Relaxation time distributions (RTDs) of saturated and desaturated capillary bundles with different cross sections: (a) circle, (b) equilateral triangle, and (c) right-angled triangle with sharp angle $\gamma_s = 10^\circ$. Each bundle is characterized by a lognormal distribution with a mean equivalent pore radius r_{eq} of 10 μm and a standard deviation of $\sigma = 0.2$ at the logarithmic scale. Nuclear magnetic resonance (NMR) signals were computed for $\rho_2 = 10$ μm s^{-1} with a noise level of 0.1% and inverted using the linear least square (LLS) approach

latter one represents the new relaxation regimes that are developing in form of the meniscus water in the corners. In the third case (right-angled triangular cross-section), a monomodal distribution similar to the circle case also appears after desaturation. However, for the right-angled triangle, the desaturated spectrum lies partly outside the original saturated RTD (Figure 3c). This is because the relaxation spectrum is formed by an overlap of the signals from the pores that are still completely saturated and those from the meniscus water in the sharp-angled corners of the desaturated pores. In addition, we note that any signal from the other two angles have apparently disappeared from the RTD, because their contribution is so small that it is completely smeared to zero by the smoothness regularization of the LLS algorithm.

It is worth noting that, for a bundle of triangular pores, the NMR response of the remaining water in the corners is always the same regardless of the original pore size. This is because the response of a corner only depends on the ratio P_C/A_C, which is related to the angle of the corner and the predominating pore pressure that corresponds to r_{menis} (Table 1).

2.4 | Hydraulic conductivity of single capillaries and corners

The hydraulic conductivity of arbitrary ducts can be calculated, given that the geometry of their cross-sectional flow area is constant in flow direction and can exactly be parameterized, by combining Darcy's law with analytical or numerical solutions determining the mean flow velocity through the cross-section of the duct (see, e.g., Patzek & Silin, 2001; Tuller & Or, 2001). The result is an expression with the following structure:

$$K_{duct} = \frac{\rho g}{\eta_0} k = \frac{\rho g}{\eta_0} \frac{1}{\kappa} L^2 \tag{4}$$

with g (in m s^{-2}) being the gravitational acceleration, and ρ (m^3 kg^{-1}) and η_0 (kg m^{-1} s^{-1}) being the density and dynamic viscosity of the pore water, respectively. The permeability term k is a function of the pore space characteristics (i.e., pore dimension L and the nondimensional flow resistance parameter κ; Patzek & Silin, 2001; Ransohoff & Radke, 1988; Tuller & Or, 2001), which depends on the individual cross-sectional geometry of the capillary or duct. Table 1 lists the corresponding k of the capillaries and corners used in this study.

Patzek and Silin (2001) showed that the hydraulic conductivity of capillaries with arbitrary triangular cross-section can be approximated using the relation

$$K_{triangle} \sim \frac{\rho g}{\eta_0} \frac{3G}{5} A_0 \tag{5}$$

with the shape factor G being the ratio of the triangle area and its squared perimeter (i.e., $G = A_0/P_0^2$). Our solution for the right-angled triangle is based on this approximation.

The hydraulic conductivity of the remaining meniscus water in a corner, after air has entered an angular capillary, depends on r_{menis} and the angle γ of this corner. Ransohoff and Radke (1988) have numerically calculated the corresponding flow resistance for discrete angles. Based on these values, Tuller and Or (2001) suggested an interpolating parameterization

$$\varepsilon(\gamma) = \exp\left(\frac{b + d\gamma}{1 + c\gamma}\right)$$

with $b = 2.124$, $c = -0.00415$, and $d = 0.00783$ that is valid for angles in the range $\gamma \in [10^\circ, 150^\circ]$. We set the sharp angle γ_s of the right-angled triangle capillary to 10°, which marks an endmember regarding its angularity within the valid range for calculating the corresponding conductivity.

2.5 | Parameterization of the WRF

The capillary pressure curve, a term that is frequently used in reservoir rock physics, describes the relationship between pore saturation and pore pressure. Equivalent soil physical descriptions define the WRF and include, in general, not only capillary forces but also the water that is kept by adsorptive forces. Although these two terms are often treated as synonyms in literature, we want to distinguish them carefully to avoid misinterpretations. As mentioned above, the WRF considers the total water saturation S_{tot} consisting of two proportions of water: S_{cap} is the proportion captured by capillary forces, and S_{ad} is the other one captured by adsorptive forces:

$$S_{tot}(h) = wS_{cap}(h) + (1-w)S_{ad}(h) \tag{6}$$

where w is an empirical weighting factor ($w \in [0,1]$) and h is the suction (in cm H_2O), that is, the amplitude of the pore pressure head normalised to values of heights.

In this study, we follow the suggestion of Peters (2013), who, by introducing the two helping functions $\Gamma(h)$ and $X(h)$, describes the total saturation S_{tot} by

$$S_{tot}(h) = w\Gamma(h)X(h) + (1-w)X(h) \tag{7}$$

Although $\Gamma(h)$ can be any kind of either empirical or physical model parameterization of the capillary pressure curve, the function $X(h)$ describes the S_{ad} part with

$$X(h) = \begin{cases} X_m\left[1 - \frac{\ln(1+h/h_a)}{\ln(1+h_0/h_a)}\right], & \text{for } h > h_a \\ 1, & \text{for } h \le h_a \end{cases} \tag{8}$$

$$X_m = \left[1 - \frac{\ln(2)}{\ln(1+h_0/h_a)}\right]^{-1}$$

The specific suctions h_0 and h_a are fix points: at h_0, the water content of the medium equals 0, and below h_a, $X(h)$ equals 1. From a thermodynamic point of view, h_0 can reliably be fixed at 6.3×10^6 cm as demonstrated by Schneider and Goss (2012). They have shown that this suction corresponds to a dehydration at 105 °C, a temperature at which soil samples usually lose their pore water completely. h_a is in principle a pure empirical fitting parameter without physical meaning. However, also for this value a natural threshold exists: it cannot be smaller than the air entry value of the medium under study. Peters (2013) suggests, for the sake of simplicity, to fix h_a at the suction corresponding to the median pore radius of the capillary pressure curve (at the logarithmic scale).

One of the objectives of this study is the estimation of $\Gamma(h)$ from NMR relaxation data. However, we also use the empirical model of van Genuchten (1980), referred to as the VG model in the following, to parameterize $\Gamma(h)$ for testing our NMR-based estimates:

$$\Gamma(h) = \left[\frac{1}{1+(\alpha h)^n}\right]^m \tag{9}$$

The parameters α, n, and m are fitting parameters. We use the so-called constraint form of the VG model with $m = 1 - 1/n$. Originally, the VG model is defined using an asymptotic residual water content as a proxy for the adsorbed water content. However, following the argumentation of Peters (2013), we substitute this asymptote by the function $X(h)$ according to Equations 7 and 8, which is more plausible from a physical point of view.

Using the VG parameterization, we calculate the relative hydraulic conductivity K_{rel} according to Mualem (1976), referred to as VGM from now on:

$$K_{rel} = \frac{K_U}{K_S} = \sqrt{\Gamma(h)}\left\{1 - \left[1 - \Gamma(h)^{1/m}\right]^m\right\}^2 \tag{10}$$

where K_S and K_U are the saturated and unsaturated conductivities, respectively.

Reviewing Equation 7, we note that $S_{cap}(h)$ in the model is actually the factor of the capillary pressure model $\Gamma(h)$ and $X(h) = S_{ad}(h)$. According to Peters (2013) this is a necessary correction to guarantee that S_{cap} decreases to 0 with increasing h at the very dry range. At the wet range and near saturation, the impact of this correction is negligible. Peters (2013) shows for a broad range of examples that this model describes WR data much more plausibly than models using the concept of an asymptotic residual water content.

3 | MATERIALS AND METHODS

3.1 | Measurements of NMR and WR

We use the same materials as in a preceding study (Costabel & Yaramanci, 2011) to test the performance of the estimation approaches suggested in this paper (i.e., sands with varying grain sizes from fine to coarse; see Table 2). Samples were prepared in cylindrical plastic tubes (diameter: 3.6 cm, height: 5.5 cm) with microfiber filters at top and bottom, which allow the connection to a self-constructed pipe system for performing flow experiments. The samples were saturated using deionized water (from bottom to top) and weighed. Their (saturated) hydraulic conductivities K_S were determined with constant head experiments.

TABLE 2 Textural and soil hydraulic information of the investigated sample material

Parameter	Fine sand (FS)	Medium, fine sand (MSFS)	Medium sand (MS)	Coarse sand (CS)
Grain size, mm	0.06–0.2	0.15–0.4	0.25–0.5	1.00–2.00
Φ^a, $cm^3\ cm^{-3}$	0.43	0.39	0.39	0.37
$K_S{}^a$, cm d−1	713 ± 8	2,103 ± 70	6,212 ± 265	10,868 ± 144
n^a	5.30 ± 0.96	2.28 ± 0.79	2.09 ± 0.47	2.18 ± 0.60
α^a, cm^{-1}	0.02 ± 0.00	0.05 ± 0.03	0.14 ± 0.12	0.13 ± 0.12
w^a	0.91 ± 0.02	0.84 ± 0.03	0.92 ± 0.02	0.88 ± 0.02
Φ^b, $cm^3\ cm^{-3}$	0.42 ± 0.01	0.39 ± 0.01	0.39 ± 0.00	0.38 ±0.02
$K_S{}^b$, cm d−1	268 ± 112	1,529 ± 104	6,713 ± 804	40,392 ± 2,428
n^b	2.82 ± 1.39	3.60 ± 0.60	6.11 ± 1.02	6.60 ± 1.61
α^b, cm^{-1}	0.02 ± 0.01	0.02 ± 0.00	0.04 ± 0.00	0.18 ± 0.01
$S_R{}^b$	0.21 ± 0.01	0.09 ± 0.00	0.09 ± 0.00	0.12 ± 0.01
Φ^c, $cm^3\ cm^{-3}$	0.43–0.45	0.34–0.36	–	0.39–0.43
n^c	12.4–14.7	4.6–7.6	–	9.8–13.3
α^c , cm^{-1}	~0.02	0.04–0.06	–	0.10–0.13
$S_R{}^c$	0.10–0.11	0.05–0.07	–	0.07–0.12

Note. Φ, porosity; K_S, saturated hydraulic conductivity; n and α, van Genuchten parameters, S_R, residual saturation degree.

[a]Measurements and estimations in this study, see text for details.

[b]Data from Costabel and Yaramanci (2011): estimates from inverse modeling of drainage experiments.

[c]Unpublished data, results from evaporation experiments.

The samples were placed inside the NMR device (Maran Ultra, Resonance Instruments) for the initial T_2 experiments, which were conducted using the Carr–Purcell–Meiboom–Gill (CPMG) sequence (Dunn et al., 2002) with an echo spacing of 150 μs. The number of scans (= measurement repetitions) was set to 100, and the total recording time was individually adjusted such that the measurement curve relaxes to a level smaller than the noise (i.e., about 1–6 s). Afterwards, the samples were successively desaturated using a pressure plate apparatus (Warrick, 2003). Different pressures were applied according to the suction range from $h = 63$ to 1,995 cm. The corresponding S_{tot}–h data pairs, where S_{tot} was determined by weight, were used as references for verifying the NMR-based WRF estimations. The CPMG measurements were conducted at the first ($h = 63$ cm) and at the last ($h = 1{,}995$ cm) desaturation step. To account for the decreasing signal strength with decreasing saturation, the number of scans was increased to the maximum value of 900 at $h = 1{,}995$ cm.

To obtain continuous reference curves for WRF and K_{cap}, the measured S_{tot}–h data pairs were fitted using Equation 7 with $\Gamma(h)$ parameterized by the VGM model (Equations 9 and 10). Table 2 lists the specifications of our samples as measured in this study, the corresponding hydraulic parameterizations, and, in addition, results of hydraulic parameterizations from other experiments using different specimen of the same material for comparison.

3.2 | NMR data processing and interpretation

3.2.1 | NMR data inversion

The flowchart in Figure 4 sketches the main processing steps to obtain a sample's PSD, WRF, and capillary-based hydraulic conductivity K_{cap}. The main step in this procedure is the determination of the PSD by a so-called joint inversion of at least two NMR relaxation signals at different saturation states with known h. All NMR data were processed using the open-source software NUCLEUS (Hiller, 2020), which includes the joint inversion approach of Hiller and Klitzsch (2018) that is also used in this study. This approach uses pores with either cylindrical or angular cross-sections and combines two or more NMR relaxation measurements at different partial saturations in one single inversion problem. By doing so and given that the pressure head for each partial saturation step is known, the surface relaxivity ρ_2 (see Equation 3) is included as a fitting parameter and is estimated without an additional empirical calibration step. This procedure provides the benefit that the PSD is automatically determined as inversion result. However, this comes at the cost of a much more complex (because nonlinear) inversion procedure (Hiller & Klitzsch, 2018; Mohnke, 2014). For the implementation details of the joint inversion approach, we refer the reader to Hiller and Klitzsch (2018).

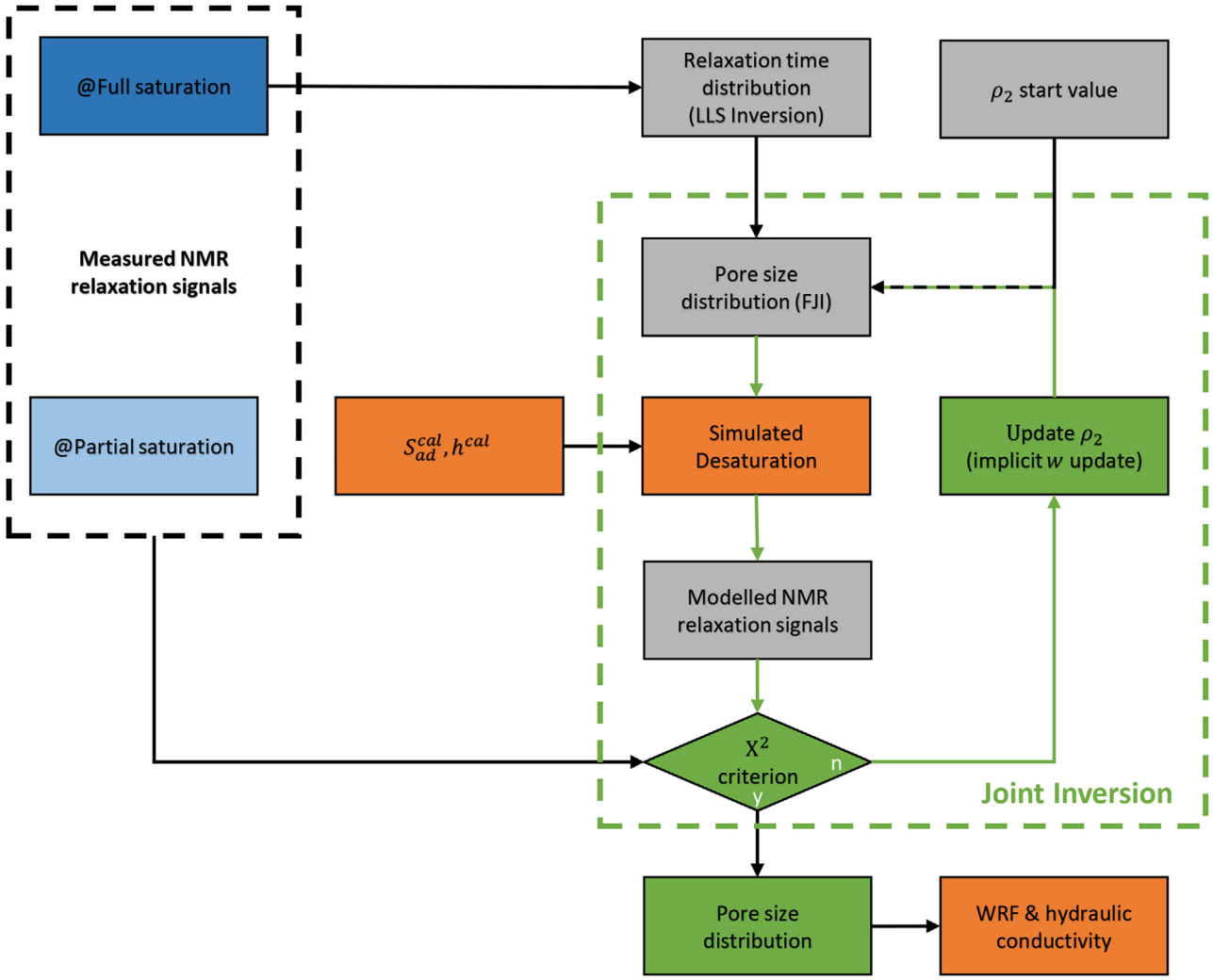

FIGURE 4 Flowchart demonstrating the joint inversion of nuclear magnetic resonance (NMR) and saturation data to derive the sample's pore size distribution (PSD) from which the water retention function (WRF) and hydraulic conductivity are estimated. LLS, linear least square; ρ_2, surface relaxivity; FJI, fixed joint inversion; S_{ad}^{cal} and h^{cal}, calibration parameters; w, empirical weighting factor

We apply the joint inversion in its basic form and combine the data of the saturated sample (at h_1) and that of one partial saturation state (h_2) to estimate the PSD. However, depending on the desired accuracy and the complexity of the pore space, it might be beneficial to use more than one NMR dataset at partial saturation (Hiller & Klitzsch, 2018; Mohnke, 2014), i.e., to apply more desaturation steps h_j with $j > 2$ using the so-called free joint inversion protocol. Instead, we use the protocol of the fixed joint inversion (FJI; Hiller & Klitzsch, 2018), for which one desaturation step is sufficient. For the FJI, ρ_2 is the only fitting parameter. This implies that the geometry of the capillary cross-section (i.e., circle, equilateral triangle, or right-angled triangle with its corresponding sharp angle γ_s) has to be defined beforehand and is constant throughout the data inversion.

The first step within our inversion protocol is the determination of the RTD of the NMR signal at $h_1 = 0$ cm (full saturation) by means of a standard LLS inversion. Based on arbitrary starting values for ρ_2, the RTD is transformed into a PSD (i.e., the corresponding intensity distribution $I_i\,[T_2]$ is reinterpreted as a function of the characteristic pore size L as defined in Figure 1, a–c). Subsequently, the desaturation related to h_2 is simulated for the PSD: all pores with $h_{crit} > h_2$ remain saturated, whereas for the pores with $h_{crit} \leq h_2$ the amount of the remaining water in the menisci is calculated. The original protocol according to Hiller and Klitzsch (2018) is slightly modified here to implement $X(h)$ for a realistic WRF reconstruction (Equations 7 and 8). The inclusion of $X(h)$ as part of the iterative fitting process is necessary for the water balance and results in the final determination of the weighting factor w between $X(h)$ and $\Gamma(h)$. However, this aspect is independent of the NMR forward operator, because we do not consider the NMR relaxation of the corresponding water films. More details on calibrating $X(h)$ are given below in Section 3.2.2.

After simulating the desaturation at h_2, we model the theoretical NMR response of the still saturated pores plus the contribution of the meniscus water and compare it to the actual NMR relaxation signal at h_2. We use a χ^2 criterion to evaluate the quality of the inversion (Aster, Borchers, & Thurber, 2013), meaning we calculate the residual of measured and modeled NMR data and relate it to the actual noise level. A value of $\chi^2 = 1$ indicates a reliable inversion result within the error bounds of the underlying data. If χ^2 is larger than 1, then the model (PSD) is in general "too smooth" and the data misfit is large. If χ^2 is smaller than 1, the inversion misinterprets noise as data and yields a "rough" inversion model, typically a rather unphysical multimodal PSD. If the χ^2 criterion is satisfied, the current PSD is accepted to be the optimum solution. Otherwise, the procedure is iteratively repeated with corresponding updates of ρ_2 until the PSD result is acceptable or the convergence criterion is reached. Finally, WRF and hydraulic conductivity are calculated.

3.2.2 | WRF reconstruction from NMR-based PSD

The joint inversion described above provides the NMR-based PSD (i.e., the intensities I_i; Equation 1) as a function of the pore size defined in Figure 1 and Table 1. From a PSD with M pore classes, $\Gamma(h)$ (Equation 7) is determined by

$$\Gamma\left(h_N\right) = \frac{\sum_{i=1}^{N} I_i + \sum_{i=N+1}^{M} \sum_{c=1}^{3} \frac{A_{c,i}}{A_{0,i}} I_i}{\sum_{i=1}^{M} I_i} \tag{11}$$

where the index N refers to an arbitrary position of Γ on the h axis and marks the largest capillary class in the bundle that is still saturated at the corresponding h_N, i is the running index, and c refers to the number of the triangle corners. It is important to note that $\Gamma(h_N)$ is the cumulative form of the PSD only in the case of the circular pores, because only in this case all pores with $h_{crit} \leq h_N$ are empty and do not contribute to the total saturation. In the case of the triangular pores, for each h_i also the meniscus water in the pores with $h_{crit} \leq h_N$ has to be considered.

In contrast to $\Gamma(h)$, any information on $X(h)$ (see Equations 7 and 8) is not available in the NMR data as long as the sample is saturated. Adsorptive water is in a permanent diffusional exchange with the interior of the pore and thus cannot be distinguished from the rest of the pore water. In order to reconstruct a reliable WRF, we have to include the $X(h)$ part by the semiempirical model introduced with Equations 7 and 8. Following the suggestion of Peters (2013) to determine h_a to be the median of the PSD model of Kosugi (1996), we implement Equation 8 by choosing h_a corresponding to the maximum of the NMR-based PSD estimation [i.e., to the inflection point of the corresponding $\Gamma(h)$]. In case of a lognormal PSD, our approach and the one of Peters (2013) lead to the very same result.

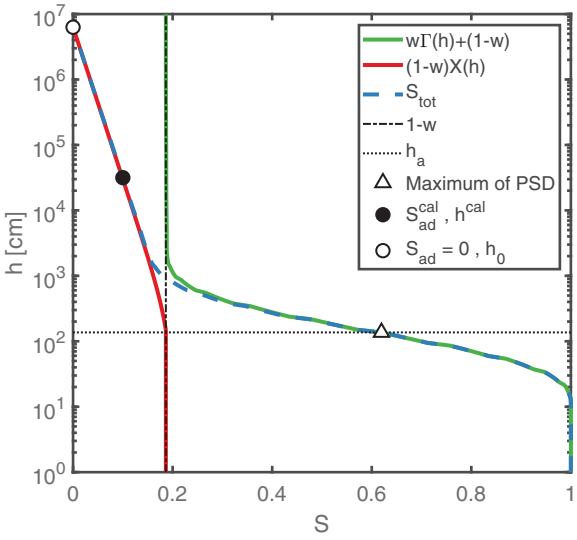

FIGURE 5 Synthetic data example demonstrating the estimation of the water retention function (blue dashed line) from the nuclear magnetic resonance (NMR)-based capillary pressure curve $\Gamma(h)$ (green solid line) according to Peters (2013) with h_a corresponding to the inflection point of the pore size distribution (PSD). $X(h)$ represents the adsorptive water saturation (red solid line), which is reconstructed with the help of two fixed points outside the capillary range: a special calibration point[S_{ad}^{cal}, h^{cal}] and the thermodynamic limit [$S_{ad} = 0$, $h_0 = 6.3 \times 10^6$ cm] for the adsorptive water proportion. S_{tot} represents the total saturation degree. For details, please see the text

Figure 5 shows an example to demonstrate how the different terms in Equation 7 are combined to form the final model of $S_{tot}(h)$ and how we implement and calibrate the $X(h)$ part. In addition to the NMR measurement at partial saturation for determining $\Gamma(h)$ by the joint inversion as described above, a calibration point (S_{ad}^{cal}, h^{cal}) for $X(h)$ is necessary. This point and the fix point at $h_0 = 6.3 \times 10^6$ cm define the slope of $X(h)$ in the semilogarithmic S–h domain. During the joint inversion, the iterative update of ρ_2 causes a shift of $\Gamma(h)$ along the h axis. The consequence of linking the parameter h_a to the inflection point of $\Gamma(h)$ is an implicit update of h_a and thus an update of the weighting factor w between $X(h)$ and $\Gamma(h)$ in each iteration step. Hence, w is implicitly determined during the NMR joint inversion.

The location of the calibration point (S_{ad}^{cal}, h^{cal}) has to be outside the capillary range. Otherwise, the residual saturation is still dominated by capillary forces (see Figure 5). In this study, the highest suction applied in the desaturation experiment is used for this purpose (h = 1,995 cm). A NMR measurement has been taken at this desaturation step, and the calibration value for S_{ad}^{cal} has been taken from it (Equation 2). However, our approach does not necessarily

require an additional NMR measurement in the dry range. A simple weighing to determine the saturation would be sufficient. The NMR data at $h = 1{,}995$ cm in this study are captured solely for demonstrating how the RTDs develop with decreasing saturation.

3.2.3 | K_{cap} estimation by parallel connection of capillaries

We observe the water flow through a bundle of parallel capillaries. Let M be the total number of the involved capillary size clusters and i the index for a certain capillary size in the bundle. As described above for a single capillary with circular or angular cross-section (Equation 4, Table 1), the hydraulic conductivity of the ith saturated circular or angular capillary (K_i) can be calculated using an equation of the form

$$K_i = \frac{\rho g}{\eta_0} \frac{1}{\kappa} L_i^2 \tag{12}$$

where L_i is the corresponding pore dimension as defined in Figure 1. To calculate the saturated hydraulic conductivity K_S of the observed capillary bundle, the individual K_i are weighted by S_i, which is the proportion of all capillaries of the ith size in the total pore volume:

$$K_S = \frac{\Phi}{\tau} \sum_{i=1}^{M} S_i K_i \tag{13}$$

with Φ and τ being the porosity and tortuosity, respectively, and S_i being the ratio of the cross-sectional area of all capillaries of the ith cluster and the total cross-sectional area of the entire capillary bundle. For the partially saturated case at a certain suction h_N, we consider N the index for the largest capillary that remains saturated, whereas all capillaries $>N$ have already been invaded by air. The corresponding hydraulic conductivity of all remaining saturated capillaries $K_{pc}(h_N)$ is given by their parallel connection:

$$K_{pc}(h_N) = \frac{\Phi}{\tau} \sum_{i=1}^{N} S_i K_i \tag{14}$$

In case of the circular capillaries, Equation 14 directly yields the desired estimation of K_{cap}. However, pore water still kept in the corners of the angular capillaries with sizes $>N$ also contributes to K_{cap} with its individual proportion on the total volume. The hydraulic conductivity of the entire meniscus water (K_{menis}) is given with

$$K_{menis}(h_N) = \frac{\Phi}{\tau} \sum_{i=N+1}^{M} S_i \sum_{c=1}^{3} \frac{A_{c,i}}{A_{0,i}} K_{c,i} \tag{15}$$

with c being the index for the corners inside the ith (triangular) capillary. $A_{0,I}$ is the cross-sectional area of the ith capillary, and $A_{c,i}$ is that of the meniscus water in its cth corner. The final prediction of K_{cap} is given by the sum

$$K_{cap}^{pc}(h_N) = K_{pc}(h_N) + K_{menisc}(h_N) \tag{16}$$

3.2.4 | K_{cap} estimation by considering an effective capillary

The definition of an effective pore radius is a well-established soil physical and petrophysical concept (Boadu, 2000; Chapuis & Aubertin, 2003; Glover & Walker, 2009). Inside the NMR community, the logarithmic mean of the RTD (Keating & Knight, 2008; Kenyon, 1997; Mohnke & Yaramanci, 2008) and the NMR-based PSD (Hiller & Klitzsch, 2018; Mohnke, 2014) is frequently used as an effective quantity to estimate the saturated hydraulic conductivity or permeability. In this study, we also want to test the performance of using the log mean as effective hydraulic quantity to predict K_{cap}. Let L_{eff} be the log mean of the saturated part of the capillary bundle at h_N, calculated by

$$\log_{10}(L_{eff}) = \sum_{i=1}^{N} \frac{S_i}{\sum_{i=1}^{N} S_i} \log_{10}(L_i) \tag{17}$$

We assume the hydraulic conductivity corresponding to L_{eff}, when computed with Equation 17, to be a reliable approximation for the entire saturated capillary bundle:

$$K_{eff}(h_N) = \frac{\Phi}{\tau} \frac{\rho g}{\eta_0} \frac{1}{\kappa} L_{eff}^2(h_N). \tag{18}$$

In the case of triangular capillaries, the water in the corners of the desaturated part of the bundle is considered in the same way as described above for the parallel connection approach:

$$K_{cap}^{eff}(h_N) = K_{eff}(h_N) + K_{menisc}(h_N) \tag{19}$$

At the end of this section, it is worth noting that the set of Equations 13–19 can provide exact estimates of hydraulic conductivity only if Φ and τ are known. Regarding the NMR method, providing reliable estimates of Φ is not a problem: it can simply be determined from the amplitude of the NMR signal of the saturated sample (Behroozmand et al., 2014; Costabel et al., 2018). On the other hand, the NMR relaxation method discussed in this study is not sensitive to τ. Thus, as an objective approximation and without being dependent on assumptions, we set $\tau = 1$. Realistic values of τ for sandy material are 2–3 (Costabel et al., 2018; Dlugosch, Günther, Müller-Petke, & Yaramanci, 2013; Hiller & Klitzsch, 2018; Mohnke, 2014) but can be much higher for finer material.

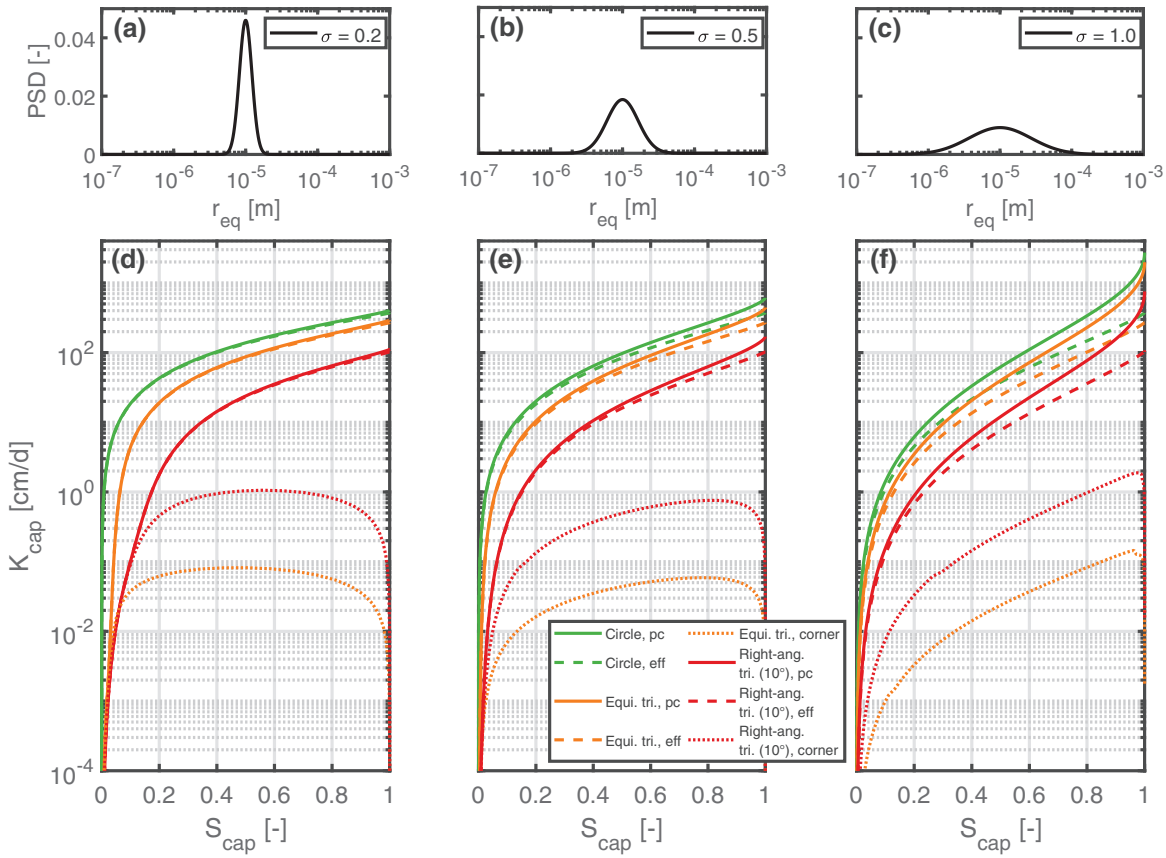

FIGURE 6 (a–c) Synthetic (equivalent) pore size distributions (PSDs) with varying broadness and (d–f) their corresponding capillary-based hydraulic conductivity (K_{cap}) estimations for different capillary cross-sections (circle, equilateral triangle, and right-angled triangle). Two approaches for the K_{cap} estimations were applied: the parallel connection (pc) of the capillary bundle and the consideration of an effective capillary (eff). r_{eq}, equivalent pore radius; S_{cap}, capillary-based saturation degree

3.2.5 | Dependency of K_{cap} estimation on capillary geometry and PSD broadness

For the comparison of the different approaches for estimating K_{cap} suggested in the section above, we consider three different synthetic PSDs with varying width. The PSDs are generated using a lognormal distribution at the r_{eq} scale (Figure 6, a–c). The median value is set to $r_{eq} = 10$ µm ($= 1 \times 10^{-5}$ m) for each of the three models and the standard deviation σ at the logarithmic scale is set to 0.2, 0.5, and 1. To demonstrate the impact of the pore angularity on K_{cap} in Figures 6d–6f, we investigate the same capillary geometries as in Figure 1: circular (green curve), equilateral triangle (orange curve), and right-angled triangle with a sharp angle of 10° (red curve). Porosity and tortuosity are set to 0.35 and 1, respectively.

As one would expect, an increasing angularity generally causes a decrease in the hydraulic conductivity, which is true for the three examples in Figure 6 and for the entire saturation range. In each case, the difference between the K_{cap} curves of the circle and the right-angled triangle is a bit more than half a magnitude, whereas the K_{cap} functions related to the equilateral triangle are relatively close to that of the circular geometry. To demonstrate the contribution of the corners, K_{menis} is depicted for the cases of the triangle capillaries (dotted lines). These curves exhibit a local maximum at saturation states <1. At the beginning of the desaturation process, only a few corners are available. With decreasing S_{cap}, the amount of corners contributing to the flow increases up to a certain point, at which the total loss of water in the flow cross-sections of the menisci predominates the process. The position of the corresponding maximum of K_{menis} strongly depends on the width of the PSD. For the narrow PSD, the maximum is reached at a medium S_{cap}. With increasing PSD width, the maximum is shifted towards higher S_{cap}.

The impact of whether handling the capillary bundle by the parallel connection (solid lines) or by assuming an effective capillary (dashed lines) for the estimation of K_{cap} is getting more and more obvious with increasing broadness of the PSD. For the narrow PSD in Figure 6d (σ = 0.2), there is no significant difference between the estimation of K_{cap}^{eff} and K_{cap}^{pc}. For broader PSDs and near full saturation, K_{cap}^{eff} is smaller than K_{cap}^{pc} by a factor of two for σ = 0.5 (Figure 6e) and five for σ = 1.0 (Figure 6f). The K_{cap}^{eff} and K_{cap}^{pc} curves converge with decreasing saturation.

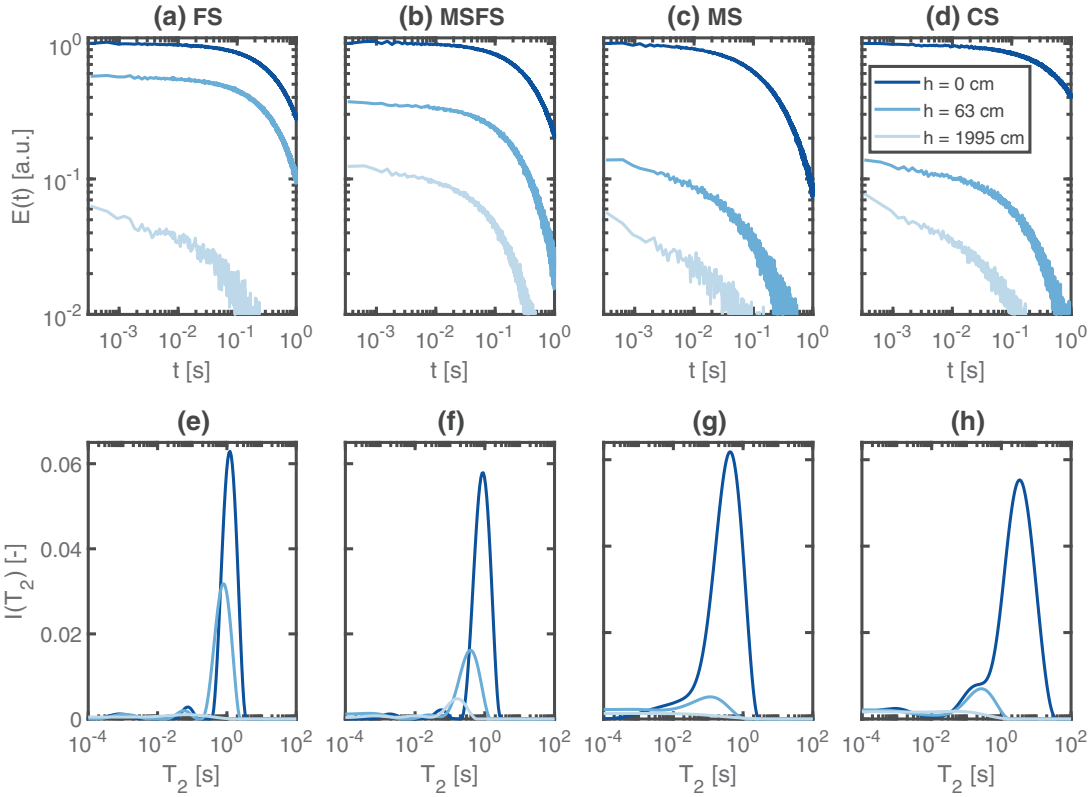

FIGURE 7 (a–d) Nuclear magnetic resonance (NMR) relaxation measurements and (e–h) their T_2 relaxation time distributions for the investigated samples and for different suctions h: fine sand (FS), medium and fine sand (MSFS), medium sand (MS), and coarse sand (CS). E(t), signal voltage; t, measurement time; $I(T_2)$, signal intensity

4 | RESULTS

4.1 | NMR relaxation data

The measured NMR data for the four samples are depicted in Figures 7a–7d along with their surface-related RTDs in Figures 7e–7h (i.e., the influence of T_{Bulk} was corrected in these RTDs). At saturation (dark blue), the two samples (fine sand [FS] and medium and fine sand [MSFS]) exhibit a simple mono-modal RTD with relaxation times symmetrically distributed around 1 s. The spectrum of the medium sand sample (MS) is also mono-modal with a maximum at about 0.4 s, but asymmetric with significant amplitudes at short relaxation times. The RTD of the coarse sand (CS) has a slightly bimodal character with a major maximum at 3 s and a minor one at 0.1 s. With respect to the data at saturation, the RTDs at $h = 63$ cm (medium blue) behave quite differently. Although for MS and CS these RTDs completely lie inside the saturated RTDs, for FS and MSFS, new relaxation regimes at T_2 times shorter than at full saturation appear during the desaturation. Along with Figure 3, it was already discussed above that this behavior can be explained by capillaries with angular cross-sections. Similar observations are described and interpreted by Costabel (2011), Mohnke (2014), and Hiller and Klitzsch (2018). For the desaturation step at $h = 1{,}995$ cm (light blue), the RTDs of FS and MSFS lie inside those of $h = 63$ cm (i.e., further relaxation regimes do not appear). In contrast, the resolution of the MS and CS data for $h = 1{,}995$ cm does not allow a reconstruction of a distinct RTD. Instead, these RTDs are smeared over three to four magnitudes at relaxation times shorter than 0.1 s.

As a next step, we will inspect the performance of the joint inversion as described in Section 3.2 in detail for our samples. On top of Figure 8, the NMR signals of our samples at $h = 63$ cm are shown together with the FJI model responses for the considered capillary geometries. For comparison, also the response from the common LLS fit is shown as well. This demonstrates how accurate the data can be approximated in the best case (i.e., without the constraints due to the hydrologic desaturation model). The resulting PSDs of the samples with respect to r_{eq} are depicted on the bottom of Figure 8, whereas the corresponding estimates of ρ_2 and w are listed in Table 3.

Inspecting the results in Figures 8a and 8b, we note that the FJI approach using the triangle cross sections leads to the best approximations for FS and MSFS with acceptable data fits ($\chi^2 < 2$) except for the equilateral triangular geometry for the MSFS sample. The circular capillary does not seem to be a reliable pore space model for these two sands, because the corresponding χ^2 values exceed the inacceptable tolerance of 2.

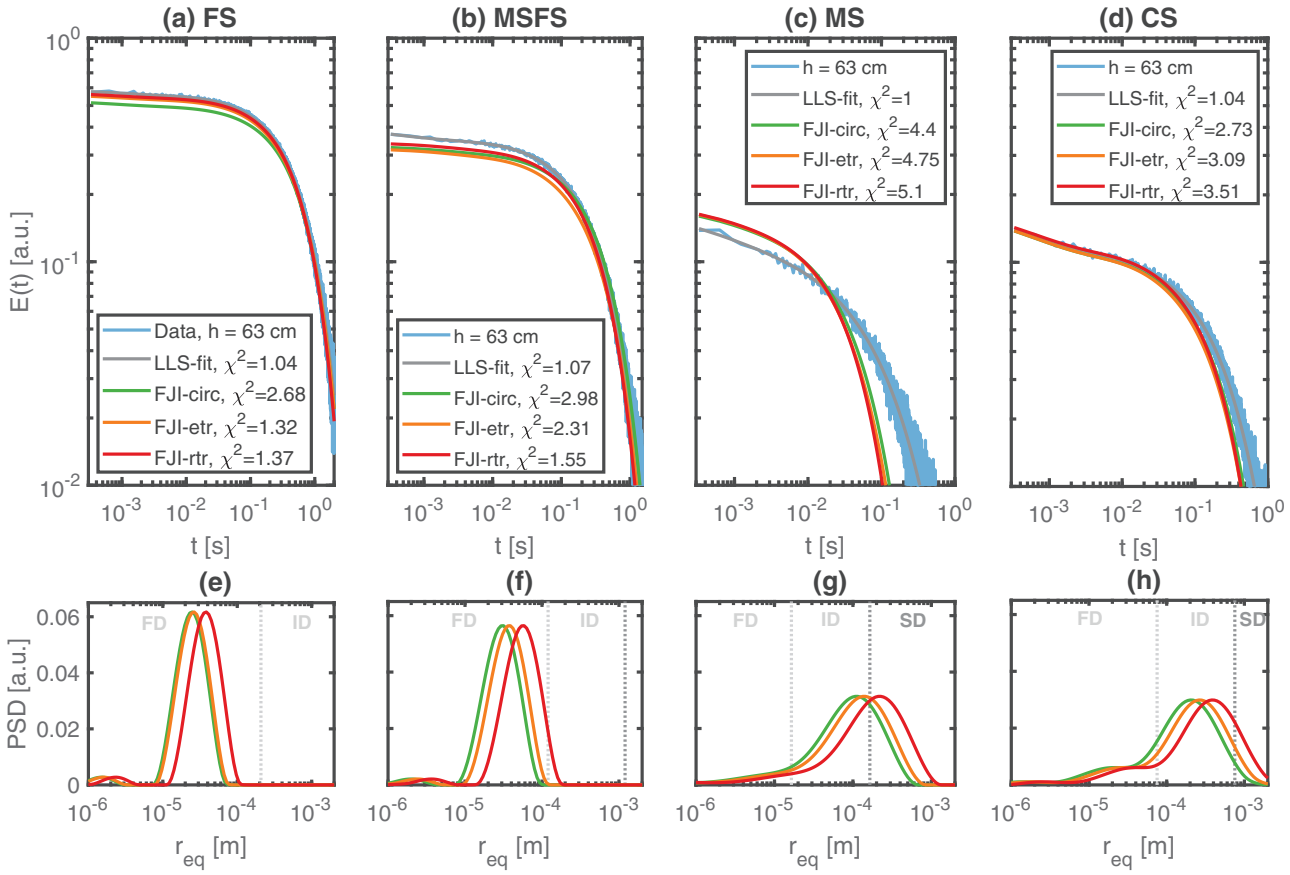

FIGURE 8 (a–d) Nuclear magnetic resonance (NMR) data for the investigated samples at partial saturation (suction [h] = 63 cm) and the corresponding model responses after applying the joint inversion using different capillary cross-sections, and (e–h) resulting pore size distributions (PSDs). The dashed lines within Subfigures e–h represent the diffusion regimes corresponding to the inverted surface relaxivities: fast diffusion (FD), intermediate diffusion (ID), and slow diffusion (SD). FS, fine sand; MSFS, medium and fine sand; MS, medium sand; CS, coarse sand; LLS, linear least square; FJI, fixed joint inversion; circ, circular model; etr, equilateral triangle model; rtr, right-angled triangle model; r_{eq}, equivalent pore radius; χ^2, quality criterion of NMR data inversion

This is also true for the samples MS and CS, no matter what cross-sectional geometry is used in the joint inversion. The data fits for these samples are imperfect with best χ^2 values of 4.4 (MS) and 2.7 (CS) for the circular capillary.

For the samples MS and CS, we note that the joint inversion approach does not work well, for neither circular nor angular cross-section, and the angularity has no significant impact on the results. Most likely, this problem is caused by the fact that at least some parts of the pore space are outside the fast diffusion region. The subfigures on the bottom of Figure 8 show, in addition to the PSD estimation for the different pore geometries, the thresholds for fast (FD), intermediate (ID), and slow diffusion (SD) regimes in the gray vertical dashed lines as computed according to Brownstein and Tarr (1979) using the circular capillary. For the samples MS and CS, it is obvious that large parts of their PSDs lie in the intermediate and/or slow diffusion region, where large pores exhibit additional relaxation modes at short T_2 times. These are misinterpreted as being small pores (Brownstein & Tarr, 1979; Costabel et al., 2018; Müller-Petke et al., 2015). In this case, the joint inversion automatically tries to include these apparent "ghost pores" in the capillary bundle, and thus it cannot reproduce the correct response for the NMR measurement at $h = 63$ cm.

For the samples FS and MSFS, which are almost completely in the fast diffusion range, we observe that the data fit using triangular capillaries leads to better results than using the circular geometry as already described above.

4.2 | NMR-based estimation of WRF

The results of the WRF estimations based on the joint inversion results are depicted in Figures 9a–9d, together with the reference data for each sample: the measured S_{tot}–h data pairs for the investigated desaturation steps (black bullets) and their corresponding WRF parameterized according to Peters (2013) and the VG model (dashed lines). The reference data are in good agreement with the NMR-estimated curves, and we observe that the joint inversion results based on the

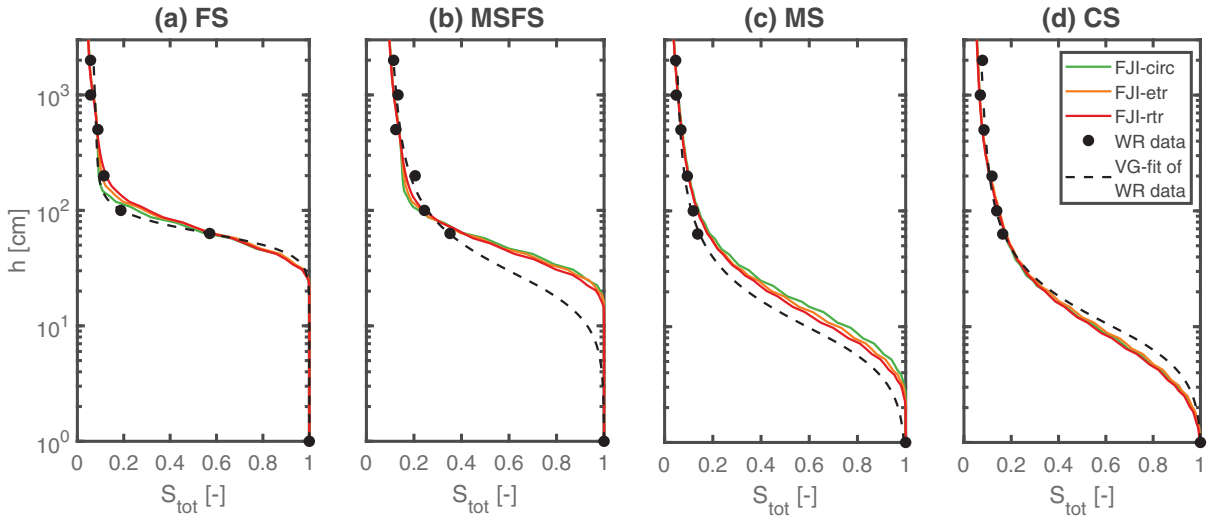

FIGURE 9 Nuclear magnetic resonance (NMR)-based estimations of the water retention functions (WRF) for the investigated samples compared to reference data: water retention (WR) measurements using a pressure plate (black bullets), and WRF reconstructed from their parameterizations using the models of Peters (2013) and van Genuchten (1980) (dashed lines). FS, fine sand; MSFS, medium and fine sand; MS, medium sand; CS, coarse sand; h, suction; S_{tot}, total saturation degree; LLS, linear least square; FJI, fixed joint inversion; circ, circular mode; etr, equilateral triangle model; rtr, right-angled triangle model; VG, van Genuchten

TABLE 3 Comparison of the linear least square (LLS) and fixed joint inversion (FJI) results for the investigated samples

		Inversion method			
Sample[a]	**Parameter**[b]	**LLS**	**FJI-circ**	**FJI-etr**	**FJI-rtr**
FS	χ^2 ($h = 0$ cm)	0.99	0.99	0.99	0.99
	χ^2 ($h = 63$ cm)	1.04	2.68	1.32	1.37
	ρ_2, μm s^{-1}	–	9.5	8.3	7.5
	w	–	0.96	0.96	0.96
MSFS	χ^2 ($h = 0$ cm)	0.99	0.99	0.99	0.99
	χ^2 ($h = 63$ cm)	1.07	2.98	2.31	1.55
	ρ_2, μm s^{-1}	–	17.6	16.7	15.6
	w	–	0.87	0.87	0.87
MS	χ^2 ($h = 0$ cm)	1.00	1.00	1.00	1.00
	χ^2 ($h = 63$ cm)	1.00	4.24	4.62	5.00
	ρ_2, μm s^{-1}	–	120.7	124.4	120.9
	w	–	0.95	0.95	0.95
CS	χ^2 ($h = 0$ cm)	1.02	1.02	1.02	1.02
	χ^2 ($h = 63$ cm)	1.04	2.52	3.11	3.52
	ρ_2, μm s^{-1}	–	25.0	22.2	21.6
	w	–	0.96	0.96	0.95

Note. The abbreviations -circ, -etr, and -rtr refer to the underlying capillary cross-sections circle, equilateral, and right-angled triangle, respectively.

[a]FS, fine sand; MSFS, medium and fine sand; MS, medium sand; CS, coarse sand.

[b]χ^2, quality criterion of NMR inversion; h, suction; ρ_2, surface relaxivity; w, empirical weighting factor.

different pore geometries only slightly differ from one another. Only the curves for the MSFS sample diverge from the reference near saturation. It seems that the NMR curves overestimate the saturation degree in this range. However, because the reference WRF has only data in the dry range, its correctness near saturation is not evident and a higher degree of uncertainty must be expected here. The same can actually be anticipated for the reference curves of the samples MS and CS. The absence of measurement points near saturation might lead to a much smoother decrease of the saturation with increasing h, when approximated using a WRF model. Interestingly, the reference curves for MS and CS show, nevertheless, a higher degree of similarity to the corresponding NMR estimations. However, considering the fact that these two samples are at least partly outside the fast diffusion regime, we have to expect that the NMR curves might overestimate the PSD (Costabel et al., 2018) and this bias would cause WRF estimations with underestimated slope similar to the reference curves. This problem will be discussed below in detail.

4.3 | Estimation of K_{cap}

Figure 10 shows the NMR-based K_{cap} estimations as functions of S_{cap} and compares them with the reference curves (i.e., VGM parameterizations; Equation 10) for K_{rel} multiplied by the measured K_S. The main trend of the curves follows the expectations discussed above along with the numerical simulations in Figure 6. The impact of the assumed pore angularity on the K_{cap} prediction increases with decreasing S_{cap}, which is obvious, at least for the samples FS and MSFS. The corresponding differences of MS and CS are much smaller. Similar to the numerical simulations in Figure 6, we note a shift between K_{cap}^{pc} and K_{cap}^{eff} for all four samples. The shift is about a factor of two and five for FS and MSFS, respectively,

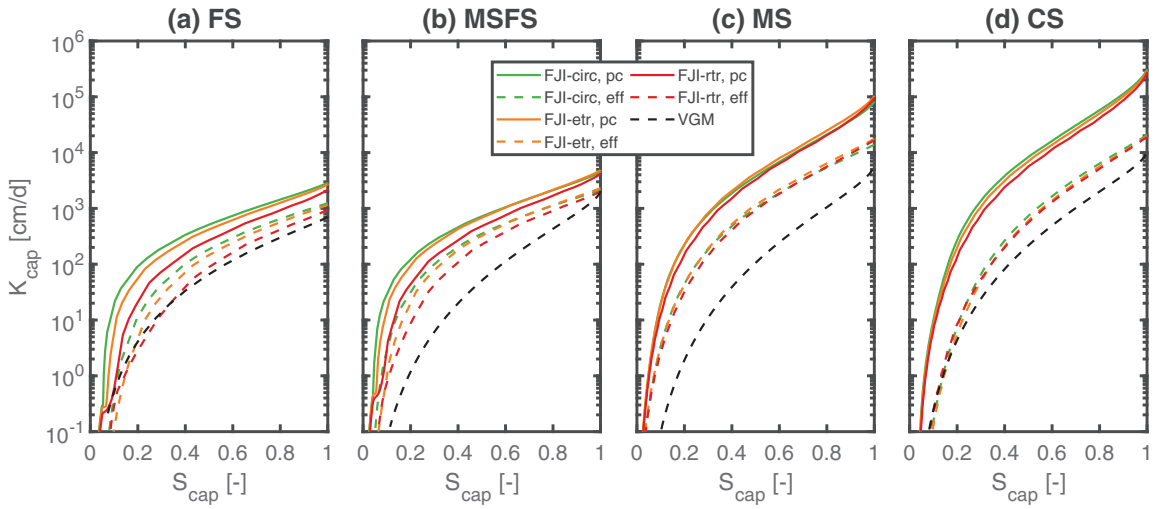

FIGURE 10 Nuclear magnetic resonance (NMR)-based estimations of the capillary-based unsaturated hydraulic conductivity K_{cap} for the investigated samples compared to reference curves estimated according to the van-Genuchten–Mualem model (VGM, dashed lines), with different capillary cross-sections (circle [circ], equilateral triangle [etr], and right-angled triangle [rtr]), and two different approaches for the K_{cap} estimations were applied: the parallel connection (pc) of the capillary bundle and the consideration of an effective capillary (eff). FS, fine sand; MSFS, medium and fine sand; MS, medium sand; CS, coarse sand; FJI, fixed joint inversion; S_{cap}, capillary-based saturation degree

and about 10 for the other two samples. Compared with the reference curves, the NMR-based K_{cap}^{pc} are larger with differences of a half to more than one magnitude over the entire S_{cap} range. The K_{cap}^{eff} estimates lead to smaller values closer to the references. Among the different investigated capillary cross sections, the right-angled triangle leads to results systematically closest to references, whereas the circle leads to the worst agreement. This is again most obvious for FS and MSFS.

5 | DISCUSSION

5.1 | Potential of WRF estimation from NMR

As described in Section 3.2, we apply the joint inversion concept of Hiller and Klitzsch (2018) to estimate the PSDs of our samples. The employed FJI protocol uses the RTDs of the saturated sample together with the NMR relaxation data at partial saturation ($h_2 = 63$ cm) for the same sample. During the inversion, the data at $h_2 = 63$ cm are approximated by linking the NMR forward modeling with a hydraulic desaturation modeling. This means we use exact physical concepts to estimate the PSDs of our samples and do not rely on additional calibration data on the surface-to-volume ratio. This is a great benefit of the joint inversion approach, but at the same time, it is also a certain limitation. The achievable accuracy of the data approximation for the desaturated sample strongly depends on the choice of the underlying capillary cross-sectional geometry, and the corresponding χ^2 criterion will achieve acceptable values only if the predetermined capillary model allows this. Using an insufficient model, the algorithm will minimize χ^2 by varying ρ_2 as well but can never reach a reliable χ^2 as can be seen for the samples FS and MSFS in case of choosing circular capillaries. In contrast, the capillaries with triangular cross sections are able to explain the measured NMR data for these two samples much better than the circular geometry. The right-angular shape with a sharp angle of 10° leads to the best data fit among the tested geometries.

For the two samples with coarse material (MS and CS), the χ^2 exceeds 2, which means the measured NMR data of the desaturated sample cannot fully be explained by the NMR forward operator. It is evident that these samples are partly outside the fast diffusion regime (Figure 8). This causes additional relaxation modes at short T_2 times that pretend to be related to smaller pores if not considered properly in the NMR forward modeling. By using the full saturation RTD, the joint inversion algorithm includes these "ghost" pores in the simulation of the desaturation and overestimates in this way the relaxation rate of the actual NMR data at partial saturation (Figures 8c and 8d). The anticipated consequence is an NMR-based PSD with overestimated width, and thus a corresponding WRF with overestimated slope. However, this systematic erroneous estimation is not very obvious for our two samples MS and CS, which are nevertheless in quite good agreement with the reference WRF. We assume that the reference curves for these samples also exhibit a bias to an overestimated slope similar to the NMR data: the corresponding WR reference data are only available in the dry range and allows too much degree of freedom for the range near saturation. Table 2 lists

VG parameters of other specimens of the same material that supports this hypothesis. In particular, the VG parameter n is much larger for these sample realizations, which indicates a WRF showing a much faster decrease of saturation with increasing h compared with our samples. An important task for future research to improve the NMR joint inversion concept and to enhance its applicability for coarse material is the inclusion of the relaxation mechanisms under intermediate and slow diffusion conditions (Brownstein & Tarr, 1979) in the forward operator. We anticipate that the observed overestimation of the NMR-based PSD can be corrected in this way. Apart from such improvements of the data inversion protocol, the experimental setup for partially saturated coarse material should be improved in future studies to account for the fact that the water content in the desaturated sample might not be homogeneously distributed. Because of its high depth resolution of about 100 to 200 µm (Costabel et al., 2018), the single-sided NMR technology seems promising in this regard.

5.2 | Considering adsorbed water in the NMR data interpretation

Our approach to predict a reliable WRF combines the NMR-based PSD estimation with the semiempirical approach of Peters (2013). In this way, we account for a certain portion of water $X(h)$ (see Equations 7 and 8) that is kept in the desaturated pore space by adsorptive forces. To do this properly, a calibration of the $X(h)$ function is necessary, which is realized by an additional S_{tot}–h data pair in the dry range. In a strict physical sense, if $X(h)$ consisted only of homogeneous water films adsorbed at the pore walls, it could easily be determined from the NMR measurement at saturation: according to Equation 3 and by choosing a certain model geometry (Table 1), the joint inversion provides an estimate of the pore surface-to-volume ratio S_w/V_w of the investigated sample. The volumetric portion of the adsorbed water films is given by the product of the h-dependent film thickness (Tuller & Or, 2001) and S_w/V_w. On the other hand, a water film of a certain thickness d_{film} produces an NMR signal with a relaxation rate of $1/T_2 = \rho_2(1/d_{film})$ and gives us the opportunity to test whether or not the hypothesis of a homogeneous film is valid at a certain h. According to Tuller and Or (2001), an adsorbed water film at $h = 1{,}995$ cm has a thickness of about 2.5 nm resulting in a relaxation time of $T_2 \leq 0.3$ ms, when assuming a γ_2 of > 10 µm s^{-1}. The simple fact that we actually measure relaxation times of at least 10 ms (see Figure 7) for our samples at $h = 1{,}995$ cm leads to the conclusion that $X(h)$ cannot solely consist of film water. Peters (2013) also suggested considering w in Equation 7 to be a fitting parameter rather than a volumetric weighting factor.

Furthermore, the discussion above demonstrates a serious limitation of assuming a capillary bundle model in NMR interpretation approaches. If $X(h)$ still contains remaining water kept by capillary forces that cannot be drained at a certain h, the pore space can no longer be considered to be consisting of straight capillary tubes with plain walls. A certain roughness (Müller-Petke et al., 2015; Or & Tuller, 2000) or fractality (Müller-Petke et al., 2015) of the pore walls or even dead-end pores need to be considered. Consequently, if the dry range of sandy soil material or soils with significant amount of clay and silt are in the focus of the investigation, NMR relaxation data alone are of limited value as long as a specific model description of higher complexity is missing. Future approaches could use pore networks or fractal pore surfaces (Xu & Torres-Verdín, 2013) and/or should be combined with other petrophysical methods sensitive to pore fluid–surface interactions.

5.3 | Potential of NMR-based estimation of K_{cap} as function of S_{cap}

At least at saturation degrees where capillary forces dominate, a strict physical interpretation of NMR relaxation data based on capillary bundles with circular or angular cross-sections and the corresponding prediction of the hydraulic behaviour seems plausible. The general observation that the achievable data approximation depends on the chosen model angularity has consequences for the K_{cap} estimation. Although our study suggests that the impact of the angularity on the WRF estimation is almost negligible, choosing an insufficient capillary cross-section might lead to a certain bias in the final K_{cap} results as indicated by the synthetic study (Figure 6). Because a decreasing angularity generally shifts the K_{cap} curve towards higher values, a model with an angularity too low might overestimate the K_{cap} and vice versa. Hiller and Klitzsch (2018) suggest and discuss the use of a particular variant of the joint inversion, which allows the angularity of the capillary cross-section to be treated as additional fitting parameter. Using and developing this idea could overcome the problem of possible biases caused by insufficient predefinition of a certain (tri-)angular pore model.

According to the findings of the synthetic parameter study in Figure 6, a significant difference between our two approaches for estimating the capillary-based unsaturated hydraulic conductivity (K_{cap}^{pc} and K_{cap}^{eff}) was expected only for samples with broad PSD. However, all of our samples, although expected to have a relatively narrow PSD, show significant shifts between K_{cap}^{pc} and K_{cap}^{eff}. The reason for this observation are small local maxima appearing at short relaxation times for all samples, also for those completely in the fast diffusion regime. These maxima, although coming with no observable impact on the WRF estimations, yield a significant impact on K_{cap}^{eff} because of their contribution on the calculation of the effective capillary (Equations 17–19).

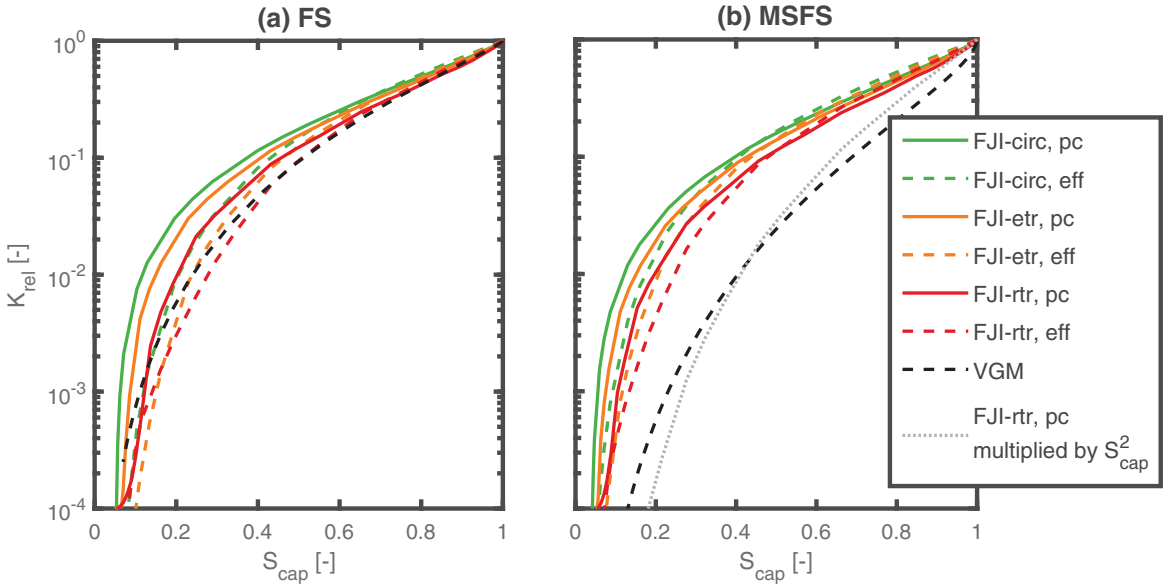

FIGURE 11 Nuclear magnetic resonance (NMR)-based estimations of the relative hydraulic conductivity K_{rel} for two investigated samples compared with the reference data (dashed lines), different capillary cross-sections (circle [circ], equilateral triangle [etr], and right-angled triangle [rtr]), and two different approaches for the capillary-based unsaturated hydraulic conductivity (K_{cap}) estimations were applied: the parallel connection (pc) of the capillary bundle and the consideration of an effective capillary (eff). FS, fine sand; MSFS, medium and fine sand; FJI, fixed joint inversion; VGM, van Genuchten–Mualem; S_{cap}, capillary-based saturation degree

However, the comparison of the NMR-based K_{cap} curves with the references illuminates another systematic effect, which is much more relevant than the assumption on the capillary cross-section. We observe in Figure 10 that both the K_{cap}^{pc} and K_{cap}^{eff} predictions tend towards overestimation. The NMR-based estimations are solely based on the flow along straight capillaries, whereas the reference curves based on the VGM model, like most of the other empirical flow models, include a tortuosity term. The tortuosity takes into account that the pore fluid flow path is not straight. It is frequently considered as a pure empirical parameter (Chapuis & Aubertin, 2003; Matyka, Khalili, & Koza, 2008; Mualem, 1976), which has to be determined by calibration or which is simply predefined by experience. Most often, the tortuosity is considered by a power law of the effective saturation (Mualem, 1976).

Considering the actual difference of K_S as measured and K_{cap}^{pc} at $S_{cap} = 1$, we can estimate the tortuosity term τ according to Equation 13. In this way, we get $\tau = 3.1$ and 2.0 for FS and MSFS, respectively, which is plausible regarding expected values for sandy material (see, e.g., Costabel et al., 2018; Dlugosch et al., 2013; Müller-Petke et al., 2015). For the other two samples, τ exceeds the plausible range by more than a factor of 10. Obviously, the occurrence of the "ghost pores" due to the relaxation outside the fast diffusion regime as described above leads to a great overestimation of K_{cap}^{pc}, which cannot be explained by a tortuosity effect.

For the samples FS and MSFS, the K_{cap}^{eff} seems to be superior to the K_{cap}^{pc} approach. The concept of using an effective capillary as a proxy for the saturated part of the pore space is able to compensate for the tortuosity effect to some extent, which is evident because the K_{cap}^{eff} curves are generally closer to the reference curves. At saturation and at least for the samples FS and MSFS, the effective capillary approach leads to a K_S estimate almost in agreement with the measured value. With decreasing S_{cap}, K_{cap}^{eff} matches with the reference curve only in case of FS, whereas for MSFS, the difference between the two increases. A tortuosity term increasing with decreasing saturation could correct this disagreement for the entire S_{cap} range.

To test this hypothesis, we finally investigate the corresponding K_{rel} estimations of the samples FS and MSFS in Figure 11. The NMR-based K_{cap} curves are normalized with respect to their individual K_S estimates and compared with the VGM references. We note that the angularity-induced differences in K_{rel} lie within half a magnitude no matter if using K_{cap}^{pc} or K_{cap}^{eff}. Compared with K_{cap}^{pc}, the K_{cap}^{eff} estimations leads to a faster decrease of K_{rel} with decreasing S_{cap}, and in this way, at least for FS and the right-angled triangle geometry, to an excellent agreement with the reference curve. For MSFS, the K_{cap}^{eff} estimations are slightly closer to the reference. An agreement between the curves can be achieved by multiplying the NMR-based estimation of K_{rel} with S_{cap}^2(example in Figure 11: the K_{cap}^{eff} estimation using the right-angled triangle geometry depicted by the gray dotted line), a saturation-dependent tortuosity-like factor similar to known empirical K_{rel} models. Of course, the water flow through a partially

saturated capillary bundle, no matter what specific geometry is assumed, cannot explain this behavior. For a strict physical explanation, pore models with a higher degree of complexity (e.g., pore networks) must be considered (Xu & Torres-Verdín, 2013).

6 | CONCLUSIONS

We present an approach to predict WRF and K_{cap} from NMR relaxation data based on physical interpretation and without the usual need of additional calibration data on the surface-to-volume ratio of the material under study. The basis of this approach is the combination of the NMR modeling with the hydraulic desaturation modeling inside a capillary bundle with either circular or triangular capillary cross-sections using the joint inversion concept of Hiller and Klitzsch (2018). So far, the model geometry has to be predetermined, which might cause a bias of the result if the chosen model angularity is insufficient. However, the usual smooth LLS inversion of the involved NMR data provides significant indications for a predominantly angular pore space: if the RTD at partial saturation lies outside the saturated RTD, a triangular model should be considered. Future versions of the joint inversion protocol should consider the angularity of the capillary cross-section as a fitting parameter.

The angularity of the used pore model has a significant impact on the predicted K_{cap} but not on the WRF estimation. At least for our sand samples in the fast diffusion regime, the NMR-based WRF estimation is reliable, whereas for samples with pores outside fast diffusion conditions, the width of the corresponding PSD is likely overestimated. Including the relaxation mechanisms for intermediate and slow diffusion in the forward operator to enhance the applicability of the joint inversion also for coarse material is an important objective for future research.

The K_{cap} estimation based on the parallel connection of the involved capillaries is reliable but leads to systematic overestimations as long as a plausible tortuosity model is not considered. Simple NMR relaxation data are not sensitive to the tortuosity. Consequently, involving a tortuosity term in the procedure would necessitate an additional empirical calibration or must be provided by additional measurements (e.g., gradient-field NMR [Latour, Kleinberg, Mitra, & Sotak, 1995; Pape, Tillich, & Holz, 2006] or electric resistivity [Archie, 1950; Shah & Singh, 2005]). The K_{cap} estimation based on the assumption of an effective capillary as a proxy for the saturated part of the bundle is able to circumvent the tortuosity problem to some extent. However, in general, the assumption of a tortuosity term and a corresponding calibration remains necessary if NMR relaxation data are the only data source of the K_{cap} estimation.

Our future research in this field will include real soils with certain contents of silt and clay and much more samples, which allows a statistical assessment of the approach. It remains an open question, how well the idea of using the NMR data at saturation for predicting WRF and K_{cap} performs in general compared with other methods such as the evaporation method, and whether or not NMR relaxometry can be considered a reliable method for supporting soil physical laboratory work.

The numerical realization of the concepts to estimate WRF and K_{cap} developed and investigated in this study will be made available to the scientific community within the open source software package NUCLEUS (Hiller, 2020).

ACKNOWLEDGMENTS

We like to thank Norbert Klitzsch and another anonymous reviewer for their fruitful critiques and discussions that helped improve the manuscript a lot.

AUTHOR CONTRIBUTIONS

Stephan Costabel: Conceptualization; Data curation; Investigation; Methodology; Writing-original draft; Writing-review & editing. Thomas Hiller: Conceptualization; Investigation; Methodology; Software; Visualization; Writing-original draft; Writing-review & editing.

CONFLICT OF INTEREST

The authors declare no conflict of interest.

ORCID

Stephan Costabel https://orcid.org/0000-0003-3103-9760
Thomas Hiller https://orcid.org/0000-0002-5581-8673

REFERENCES

Archie, G. E. (1950). Introduction to petrophysics of reservoir rocks. *Bulletin of the American Association of Petroleum Geologists*, *34*, 943–961.

Arns, C. H. (2004). A comparison of pore size distributions derived by NMR and X-ray-CT techniques. *Physica A: Statistical Mechanics and its Applications*, *339*, 159–165. https://doi.org/10.1016/j.physa.2004.03.033

Aster, R. C., Borchers, B., & Thurber, C. H. (2013). *Parameter estimation and inverse problems* (2nd ed.). Waltham, MA: Academic Press. https://doi.org/10.1016/C2009-0-61134-X

Behroozmand, A. A., Keating, K., & Auken, E. (2014). A review of the principles and applications of the NMR technique for near-surface characterization. *Surveys in Geophysics*, *36*, 27–85. https://doi.org/10.1007/s10712-014-9304-0

Bittelli, M., & Flury, M. (2009). Errors in water retention curves determined with pressure plates. *Soil Science Society of America Journal*, *73*, 1453–1460. https://doi.org/10.2136/sssaj2008.008

Boadu, F. K. (2000). Hydraulic conductivity of soils from grain-size distributions: New models. *Journal of Geotechnical and Geoenvironmental Engeneering*, 126(8). https://doi.org/10.1061/(ASCE)1090-0241(2000)126:8(739)

Brownstein, K. R., & Tarr, C. E. (1979). Importance of classical diffusion in NMR studies of water in biological cells. *Physical Review A*, *19*, 2446–2453. https://doi.org/10.1103/PhysRevA.19.2446

Campbell, G. S., Smith, D. M., & Teare, B. L. (2007). Application of a dew point method to obtain the soil water characteristic. In T. Schanz (Ed.), *Experimental unsaturated soil mechanics*. (pp. 71–77). Berlin, Heidelberg: Springer.

Chapuis, R., & Aubertin, M. (2003). *Predicting the coefficient of permeability of soils using the Kozeny-Carman equation*. Montreal, QC, Canada: Ecole Polytechnique de Montréal.

Costabel, S. (2011). *Nuclear magnetic resonance on laboratory and field scale for estimating hydraulic parameters in the vadose zone* (Doctoral dissertation, Berlin University of Technology). Retrieved from opus4.kobv.de/opus4-tuberlin/files/3173/costabel_stephan.pdf

Costabel, S., Weidner, C., Müller-Petke, M., & Houben, G. (2018). Hydraulic characterisation of iron-oxide-coated sand and gravel based on nuclear magnetic resonance relaxation mode analyses. *Hydrology and Earth System Sciences*, *22*, 1713–1729. https://doi.org/10.5194/hess-22-1713-2018

Costabel, S., & Yaramanci, U. (2011). Relative hydraulic conductivity and effective saturation from earth's field nuclear magnetic resonance: A method for assessing the vadose zone. *Near Surface Geophysics*, *9*, 155–167. https://doi.org/10.3997/1873-0604.2010055

Costabel, S., & Yaramanci, U. (2013). Estimation of water retention parameters from nuclear magnetic resonance relaxation time distributions. *Water Resources Research*, *49*, 2068–2079. https://doi.org/10.1002/wrcr.20207

Dlugosch, R., Günther, T., Müller-Petke, M., & Yaramanci, U. (2013). Improved prediction of hydraulic conductivity for coarse-grained, unconsolidated material from nuclear magnetic resonance. *Geophysics*, *78*, EN55–EN64. https://doi.org/10.1190/geo2012-0187.1

Dunn, K., Bergman, D. J., & Latorraca, G. A. (2002). *Nuclear magnetic resonance: Petrophysical and logging applications* (1st ed.). Amsterdam: Pergamon.

Glover, P. W., & Walker, E. (2009). Grain-size to effective pore-size transformation derived from electrokinetic theory. *Geophysics*, *74*, E17–E29. https://doi.org/10.1190/1.3033217

Hammecker, C., Barbiero, L., Boivin, P., Maeght, J. L., & Diae, E. H. B. (2004). A geometrical pore model for estimating the microscopical pore geometry of soil with infiltration measurements. *Transport in Porous Media*, *54*, 193–219. https://doi.org/10.1023/A:1026328706869

Hiller, T. (2020). NUCLEUS (Version v.0.1.10). Zenodo. https://doi.org/10.5281/zenodo.4022195

Hiller, T., & Klitzsch, N. (2018). Joint inversion of nuclear magnetic resonance data from partially saturated rocks using a triangular pore model. *Geophysics*, *83*, JM15–JM28. https://doi.org/10.1190/geo2017-0697.1

Ioannidis, M. A., Chatzis, I., Lemaire, C., & Perunarkilli, R. (2006). Unsaturated hydraulic conductivity from nuclear magnetic resonance measurements. *Water Resources Research*, *42*(7). https://doi.org/10.1029/2006WR004955

Jaeger, F., Bowe, S., van As, H., & Schaumann, G. E. (2009). Evaluation of ^{1}H NMR relaxometry for the assessment of pore-size distribution in soil samples. *European Journal of Soil Science*, *60*, 1052–1064. https://doi.org/10.1111/j.1365-2389.2009.01192.x

Keating, K., & Knight, R. (2008). A laboratory study of the effect of magnetite on NMR relaxation rates. *Journal of Applied Geophysics*, *66*, 188–196. https://doi.org/10.1016/j.jappgeo.2007.09.001

Kenyon, W. E. (1997). Petrophysical principles of applications of NMR logging. *The Log Analyst*, *38*, 21–43.

Knight, R., Walsh, D. O., Butler Jr., J. J., Grunewald, E., Liu, G., Parsekian, A. D., … Barrows, M. (2015). NMR logging to estimate hydraulic conductivity in unconsolidated aquifers, *Groundwater*, *54*(1), 104–114, https://doi.org/10.1111/gwat.12324.

Kosugi, K. (1996). Lognormal distribution model for unsaturated soil hydraulic properties. *Water Resources Research*, *32*, 2697–2703. https://doi.org/10.1029/96WR01776

Latour, L. L., Kleinberg, R. L., Mitra, P. P., & Sotak, C. H. (1995). Pore-size distributions and tortuosity in heterogeneous porous media. *Journal of Magnetic Resonance, Series A*, *112*, 83–91. https://doi.org/10.1006/jmra.1995.1012

Mason, G., & Morrow, N. R. (1991). Capillary behavior of a perfectly wetting liquid in irregular triangular tubes. *Journal of Colloid and Interface Science*, *141*, 262–274. https://doi.org/10.1016/0021-9797(91)90321-X

Matyka, M., Khalili, A., & Koza, Z. (2008). Tortuosity-porosity relation in porous media flow. *Physical Review E*, *78*. https://doi.org/10.1103/PhysRevE.78.026306

Mohnke, O., & Yaramanci, U. (2008). Pore size distributions and hydraulic conductivities of rocks derived from magnetic resonance sounding data using multi-exponential decay time inversion. *Journal of Applied Geophysics*, *66*, 73–81. https://doi.org/10.1016/j.jappgeo.2008.05.002

Mohnke, O. (2014). Jointly deriving NMR surface relaxivity and PSDs by NMR relaxation experiments on partially desaturated rocks. *Water Resources Research*, *50*, 5309–5321. https://doi.org/10.1002/2014WR015282

Mohnke, O., Jorand, R., Nordlund, C., & Klitzsch, N. (2015). Understanding NMR relaxometry of partially water-saturated rocks. *Hydrology and Earth System Sciences*, *19*, 2763–2773. https://doi.org/10.5194/hess-19-2763-2015

Mualem, Y. (1976). A new model for predicting the hydraulic conductivity of unsaturated porous media. *Water Resources Research*, *12*, 513–522. https://doi.org/10.1029/WR012i003p00513

Müller-Petke, M., Dlugosch, R., Lehmann-Horn, J., & Ronczka, M. (2015). Nuclear magnetic resonance average pore-size estimations outside the fast-diffusion regime. *Geophysics*, *80*, D195–D206. https://doi.org/10.1190/geo2014-0167.1

Nasta, P., Huynh, S., & Hopmans, J. W. (2011). Simplified multistep outflow method to estimate unsaturated hydraulic functions for coarse-textured soils. *Soil Science Society of America Journal*, *75*, 418–425. https://doi.org/10.2136/sssaj2010.0113

Or, D., & Tuller, M. (2000). Flow in unsaturated fractured porous media: Hydraulic conductivity of rough surfaces. *Water Resources Research*, *36* 1165–1177. https://doi.org/10.1029/2000WR900020

Øren, P.-E., Bakke, S., & Arntzen, O. J. (1998). Extending predictive capabilities to network models. *SPE Journal*, *3*, 324–336. https://doi.org/10.2118/52052-PA

Pape, H., Tillich, J. E., & Holz, M. (2006). Pore geometry of sandstone derived from pulsed field gradient NMR. *Journal of Applied Geophysics*, *58*, 232–252. https://doi.org/10.1016/j.jappgeo.2005.07.002

Patzek, T. W., & Silin, D. B. (2001). Shape factor and hydraulic conductance in noncircular capillaries. *Journal of Colloid and Interface Science*, *236*, 295–304. https://doi.org/10.1006/jcis.2000.7413

Peters, A. (2013). Simple consistent models for water retention and hydraulic conductivity in the complete moisture range. *Water*

Resources Research, *49*, 6765–6780. https://doi.org/10.1002/wrcr.20548

Peters, A., & Durner, W. (2008). Simplified evaporation method for determining soil hydraulic properties. *Journal of Hydrology*, *356*, 147–162. https://doi.org/10.1016/j.jhydrol.2008.04.016

Peters, A., Iden, S. C., & Durner, W. (2015). Revisiting the simplified evaporation method: Identification of hydraulic functions considering vapor, film and corner flow. *Journal of Hydrology*, *527*, 531–542. https://doi.org/10.1016/j.jhydrol.2015.05.020.

Ransohoff, T. C., & Radke, C. J. (1988). Laminar flow of a wetting liquid along the corners of a predominantly gas-occupied noncircular pore. *Journal of Colloid and Interface Science*, *121*, 392–401. https://doi.org/10.1016/0021-9797(88)90442-0

Schaap, M. G., Shouse, P. J., & Meyer, P. D. (2003). *Laboratory measurements of the unsaturated hydraulic properties at the vadose zone transport field study site*. USDOE. https://doi.org/10.2172/15010208

Schneider, M., & Goss, K.-U. (2012). Prediction of the water sorption isotherm in air dry soils. *Geoderma*, *170*, 64–69. https://doi.org/10.1016/j.geoderma.2011.10.008

Shah, P. H., & Singh, D. N. (2005). Generalized Archie's law for estimation of soil electrical conductivity. *Journal of ASTM International*, *2*(5). https://doi.org/10.1520/JAI13087

Šimůnek, J., & van Genuchten M.Th. (1999). Using the Hydrus-1D and Hydrus-2D codes for estimating unsaturated soil hydraulic and solute transport parameters. In M. Th. Van Genuchten & F. J. Leij (Eds.), *Characterization and measurement of the hydraulic properties of unsaturated porous media* (pp. 1523–1536). Riverside: University of California.

Skierucha, W. (2005). Design and performance of psychrometric soil water potential meter. *Sensors and Actuators A: Physical*, *118*, 86–91. https://doi.org/10.1016/j.sna.2004.08.004

Stingaciu, L. R., Weihermüller, L., Haber-Pohlmeier, S., Stapf, S., Vereecken, H., & Pohlmeier, A. (2010). Determination of pore size distribution and hydraulic properties using nuclear magnetic resonance relaxometry: A comparative study of laboratory methods. *Water Resources Research*, *46*(11). https://doi.org/10.1029/2009WR008686

Tuller, M., & Or, D. (2001). Hydraulic conductivity of variably saturated porous media: Film and corner flow in angular pore space. *Water Resources Research*, *37*, 1257–1276. https://doi.org/10.1029/2000WR900328

Tuller, M., Or, D., & Dudley, L. M. (1999). Adsorption and capillary condensation in porous media: Liquid retention and interfacial configurations in angular pores. *Water Resources Research*, *35*, 1949–1964. https://doi.org/10.1029/1999WR900098

van Genuchten, M. Th. (1980). A closed-form equation for predicting the hydraulic conductivity of unsaturated soils. *Soil Science Society of America Journal*, *44*, 892–898. https://doi.org/10.2136/sssaj1980.03615995004400050002x

Vouillamoz, J. M., Favreau, G., Massuel, S., Boucher, M., Nazoumou, Y., & Legchenko, A. (2008). Contribution of magnetic resonance sounding to aquifer characterization and recharge estimate in semi-arid Niger. *Journal of Applied Geophysics*, *64*, 99–108. https://doi.org/10.1016/j.jappgeo.2007.12.006

Warrick, A. W. (2003). *Soil water dynamics*. New York: Oxford University Press.

Xu, C., & Torres-Verdín, C. (2013). Quantifying fluid distribution and phase connectivity with a simple 3D cubic pore network model constrained by NMR and MICP data. *Computers & Geosciences*, *61*, 94–103. https://doi.org/10.1016/j.cageo.2013.08.003

How to cite this article: Costabel S, Hiller T. Soil hydraulic interpretation of nuclear magnetic resonance measurements based on circular and triangular capillary models. *Vadose Zone J*. 2021;20:e20104. https://doi.org/10.1002/vzj2.20104